Q. J. R. Meteorol. Soc. (1992), **118**, pp. 927–963 551.553.21:551.515.1:551.515.4(94)

An integrated view of the 1987 Australian monsoon and its mesoscale convective systems. I: Horizontal structure

By BRIAN MAPES and ROBERT A. HOUZE, JR.

Department of Atmospheric Sciences, AK-40, University of Washington, Seattle, Washington 98195, *USA*

(Received 17 April 1991; revised 9 March 1992)

SUMMARY

This observational study is organized around three issues: the forcing of the monsoon flow by embedded deep convection, the thermodynamic conditions that support the convection, and the structures of the mesoscale convective systems (MCSs) that constitute much of the deep convection.

The monsoon convective cloudiness occurred predominantly offshore, over the earth's warmest waters. Week-long periods of widespread deep convection caused cycles of monsoon spin-up, culminating in tropical-cyclone formation. Momentum transports by the convection also created smaller-scale vortex pairs in the upper troposphere.

Sounding data suggest that the convection was modulated by low-level processes, not by large-scale deep forced ascent. Triggering by mesoscale boundary-layer cold-pool boundaries and coastlines determined specifically where convection occurred, while several positive feedbacks acted to keep regional thermodynamic conditions favourable. Hence monsoon convection, once initiated, persisted as self-exciting 'superclusters', composed at any instant of many distinct MCSs.

The observed MCSs all contained areas of deep convection and stratiform precipitation areas. Stratiform precipitation usually evolved in place from convective cells, although precipitation also occasionally fell from overhanging anvils created by upper-level shear. The MCSs within similar *synoptic* wind environments tended to have similar *mesoscale* structures. This fact reflects the effects, illustrated herein, of environmental winds upon the relative motions of cold pools (which trigger new convective cells) and stratiform precipitation areas (which evolve from old convective cells).

1. INTRODUCTION

Deep convection in the tropics constitutes the major heat source in the global atmospheric heat engine, as pointed out by Riehl and Malkus (1958). Since then, satellite observations have made it clear that almost all tropical deep convection, even over the open oceans, is organized into mesoscale convective systems (MCSs), whose frequency of occurrence and morphology are modulated in turn by synoptic-scale circulation systems (for example, Houze and Betts 1981; Johnson and Houze 1987). Tropical cyclones are a clear example of this multiple-scale organization, with individual convective cells and stratiform rain areas organized into mesoscale eyewall and rainband structures, which are in turn organized in concentric or spiral structures relative to the cyclone. The geographically stationary mean circulation referred to herein as the Australian summer monsoon (for a review see McBride (1987)) represents a yet larger scale of organization. Within the monsoon as a whole, tropical cyclones as well as individual MCSs live out their life cycles, mostly over oceanic and coastal areas.

This paper is the first of two in which we examine the interplay of observed MCSs and the larger-scale flow during the 1987 Australian summer monsoon. We address three interlocking issues, which together shape the horizontal structure of the monsoon system: the forcing of large-scale flow by deep convection, the thermodynamic energy supply for the convection, and the processes determining the structure of the MCSs that constitute the deep convective cloudiness.

The first issue is treated in section 3, where we formulate an absolute-vorticity equation which describes the forcing of large-scale flow by deep convection. The two effects of convection on the large-scale flow, namely net heating and vertical momentum transports, appear as the two terms of the equation. The first term, often called 'vortex stretching', is shown to account qualitatively for the time-mean monsoon circulation.

The second term, the curl of an apparent force representing vertical momentum transports, tends to create vorticity couplets with no net circulation around them. The 1987 monsoon consisted of two cycles of gradual spin-up, from quiescent winds at the onset of widespread convection, to mature tropical cyclones, which in turn lasted until poleward drift took them into unfavourable environments.

The second issue is considered in section 4, in which we present a monsoon climatology of convective available potential energy (CAPE), with the contributions of boundary-layer and tropospheric conditions separately analysed. Boundary-layer humidity was the most important contributor to CAPE variations, but it varied on small horizontal and vertical scales, poorly resolved by the sounding network and even by aircraft. The upper-tropospheric contribution to CAPE variation was coherent and deep, but of small magnitude. It consisted of an intermittent warm core, hypsometrically related to the low surface pressure in the monsoon trough. More convection was observed in the reduced-CAPE, warm-core environments. Thus, low-level processes, rather than destabilization by deep forced ascent, apparently controlled the occurrence of convection. Several processes, including the inviscid heating-induced vertical circulation (often assumed, incorrectly, to consist solely of 'compensating subsidence'), acted as positive feedbacks, by which convection in an area favoured more convection nearby. The view thus emerges, supported by satellite data, that the week-long pulses of monsoon convection, once triggered, were self-exciting 'superclusters', consisting of numerous individual MCSs.

The third issue is treated in section 5. The mesoscale structures of ten well-observed MCSs are described, and the processes important to their dynamics are illustrated with data. The mesoscale horizontal structure of the MCSs is seen to arise from processes affecting the relative motions of boundary-layer cold pools (which trigger new convection) and of old convective cells, which evolve into stratiform precipitation. As a result, similar MCS structures were observed within similar synoptic-scale wind environments. In Part II, we demonstrate that the basic building blocks of MCSs, denoted 'convective', 'stratiform', and 'intermediary' precipitation areas, have similar divergence profiles in *all* the observed MCSs.

2. DATA

The data used in this study come from the jointly conducted Equatorial Mesoscale Experiment (EMEX) and Australian Monsoon Experiment (AMEX). EMEX was an aircraft-based observational program for exploring the internal structure and mesoscale dynamics of nocturnal MCSs over the tropical ocean. It consisted of airborne Doppler radar and multiple aircraft sampling in ten MCSs within the period 14 January–3 February 1987. The field-measurement phase of EMEX was conducted from Darwin, Australia (see base map, Fig. 1) during January and February of 1987. This coincided with Phase II of AMEX (Gunn *et al.* 1989) which involved an enhanced network of 6-hourly soundings (heavy dots on Fig. 1) as well as radars located at Darwin, Gove, and Weipa. The Stratospheric–Tropospheric Exchange Program (STEP) was also conducted during this time period, with flights of a US NASA ER-2 aircraft in the stratosphere above the tops of tropical cyclones and MCSs. A more general description of the EMEX program is given in Webster and Houze (1991).

The gridded fields used in this study are based on the European Centre for Medium-range Weather Forecasts (ECMWF) 12 GMT uninitialized analyses, which took as input the AMEX soundings along with the rest of the global network. We have also examined the individual AMEX soundings, provided by the Australian Bureau of Meteorology;

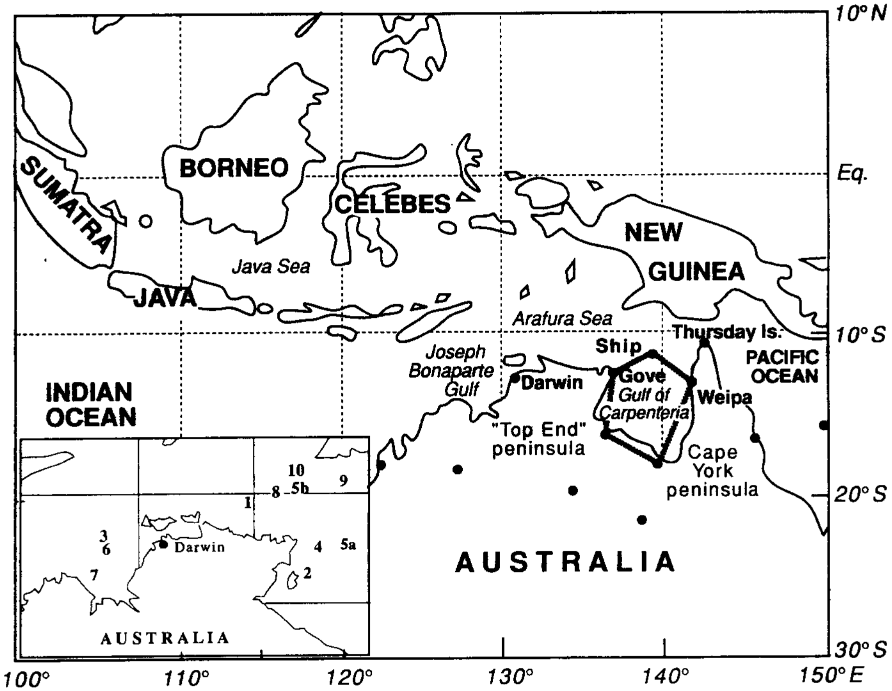

Figure 1. Base map of northern Australia and surrounding area. Heavy dots indicate AMEX sounding sites. The inset map indicates the locations of the ten EMEX aircraft missions.

the characteristics of these data are described in Gunn *et al.* (1989). Three-hourly satellite data are from the Japanese Geosynchronous Meteorological Satellite.

For the mesoscale studies, data came primarily from the three EMEX research aircraft: US National Oceanic and Atmospheric Administration (NOAA) WP-3D aircraft number N42RF (hereafter referred to as 'the P3'), the Electra aircraft of the US National Center for Atmospheric Research (NCAR), and the Australian Commonwealth Scientific and Industrial Research Organization (CSIRO) F27 aircraft. AMEX data from the Australian Bureau of Meteorology's 10 cm wavelength operational radar at Darwin were also used.

Foremost among mesoscale data sources is the P3, which was instrumented with two quantitative radars. The lower-fuselage radar has 5 cm wavelength and scans in an approximately horizontal plane, with a maximum useful range of slightly more than 100 km. It has a horizontal beam width of 1·1°, which provides a good horizontal resolution; however, it has a 4·1° vertical beam width, and thus provides values of radar reflectivity that are averages over a vertical depth that varies with range and is large at far ranges (e.g. Houze *et al.* 1981). The tail radar of the P3 has 3 cm wavelength. During EMEX, this radar scanned in the vertical plane perpendicular to the ground track of the aircraft, with a maximum range of 90 km. Doppler data from the tail radar were obtained only from 0·9 to 40 km range. Further information on the P3 and its radars can be found in Jorgensen (1984).

The following discussions of boundary-layer thermodynamics and of the structure of the EMEX MCSs have been influenced by our comprehensive examination of *in situ* data from all three aircraft. A more complete description of the EMEX aircraft and their instrumentation can be found in Gamache *et al.* (1987).

3. THE SYNOPTIC MONSOON: VORTICITY AND THE ROLE OF MCSs

In this section the first issue of this study is treated, namely the forcing of large-scale circulations by embedded deep convection. The absolute-vorticity equation provides a unifying framework for considering the two separate effects of deep convection: net heating (as reflected in divergence, an *observable* quantity) and vertical momentum transport.

The Australian summer monsoon is characterized by an intensification and southward shift off the equator of deep convective activity in the longitudes near 110–150°E, and meridional flow across the equator, from north to south at low levels and south to north in the upper troposphere. Consistent with this meridional circulation, westerly zonal winds at around 10°S in the lower troposphere, and an upper-tropospheric easterly jet over the equator, are observed. In addition, the southern hemisphere mid-latitude upper-tropospheric westerlies shift poleward. For a general review of the Australian monsoon see McBride (1987). Synoptic aspects of the 1987 Australian monsoon season have been described in Gunn *et al.* (1989), while diurnal variations have been considered in Keenan *et al.* (1989). Some speculations concerning planetary aspects of the 1987 monsoon onset have been offered by Hendon *et al.* (1989). The present analysis is focused specifically on the period encompassing the MCSs observed in EMEX.

Figure 2 shows time-series data of high cloudiness coverage (proxy for deep convection), and of the vertical profile of zonal wind component from daily average soundings at Darwin, Gove, and the EMEX ship (at 11°S, 139°E), from 10 January (day 10) to 15 February (day 46) 1987. The timings of the EMEX flights are indicated, as well as the five three-day periods—*onset*, *cyclones*, *inactive*, *second onset*, and *long zonal fetch*—to

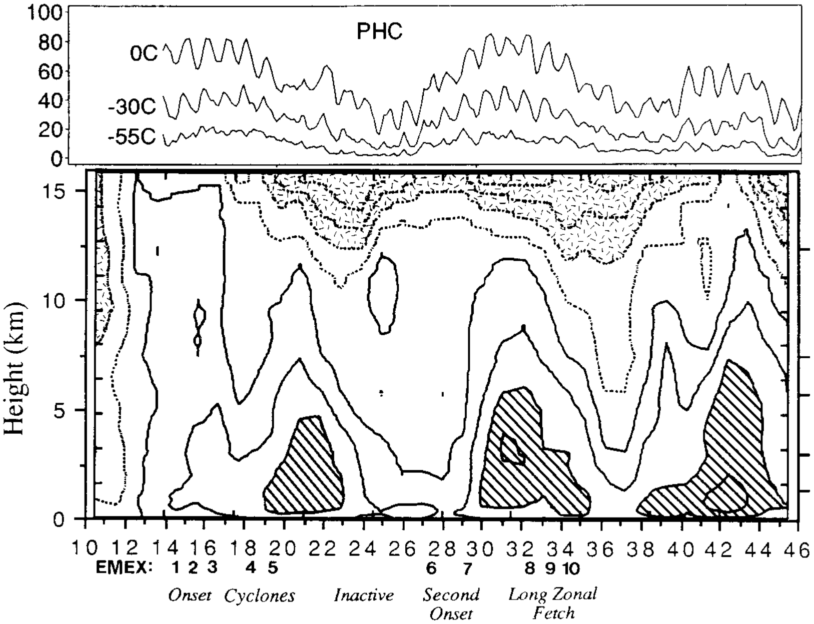

Figure 2. Time evolution of monsoon cloudiness and zonal wind component. Upper panel: regional percentage high cloudiness (PHC), defined as the fractional coverage of infrared brightness temperatures colder than the three indicated threshold temperatures, within the dashed box on Fig. 5. Lower panel: time–height section of daily-average zonal wind component in soundings from Darwin, Gove, and the ship, from 10 January (Day 10) to 15 February (Day 46) 1987. Solid contours: 0, 5, 10 (hatched) and 15 m s^{-1}; dotted contours: −5, −10 (stippled), −15 and −20 m s^{-1}. The timings of the ten EMEX aircraft missions are indicated by EMEX 1, 2, . . . 10. Five three-day named periods are also indicated.

be described below. After the sudden onset of westerly winds at all levels on 13 January, a layer of westerly zonal wind, typically extending from the surface to about 10 km altitude in active periods, tended to lag the convection in time. This time lag can be understood qualitatively by considering the westerlies as part of a monsoon-scale cyclonic circulation (trough), centred south of the soundings, that gradually intensified as the persistent divergent circulations associated with deep convection concentrated vorticity in that area.

At the surface, winds were westerly, even during the *inactive* period, spiralling cyclonically into a shallow heat low over the Australian continent. This 'dry monsoon' flow ventilated the daily solar heating of the continent, but was far weaker and shallower than the 'moist monsoon', which drew its energy from more intermittent latent heating and ultimately from the oceanic heat source (e.g. Webster 1987). In Part II, evidence will be presented that the depth of the westerly wind layer reflects the depth of the layer of convergence observed in MCSs.

(*a*) *Mean winds and cloudiness*

Figures 3 and 4 show the ECMWF-analysed mean 12 GMT fields from the period containing the ten flights of EMEX, 14 January–3 February. At 850 mb (Fig. 3(a)) there was mean cross-equatorial flow into the southern hemisphere all along the Australian longitudes. This flow curved into a mean westerly jet centred at approximately 9°S. The speed of this jet was roughly consistent with the conservation of absolute angular momentum (around the earth's axis) from a zero zonal wind speed at the equator. However, it is clear from Fig. 3(b) that the gradient of geopotential height also had a small zonal component just upstream of the jet. South of the jet lay an elongated mean trough and cyclonic circulation, with the lowest heights in the mean circulation centre located just off the north-western Australian coast. This semi-permanent circulation centre, designated the 'Australian Low' by Webster and Houze (1991), contained, during parts of the averaging period, tropical cyclones Connie and Damien, while the eastward protrusion of the mean trough reflected both an actual trough in the area from 15–18 January (see Davidson *et al.* 1990, Fig. 11(a)), and the time-averaged view of cyclone Irma moving south-westward across north central Australia from the Gulf of Carpentaria from 19 to 23 January.

At 200 mb the mean flow spiralled outward from a climatological anticyclone over Australia, north-westward across the equator, forming a tropical easterly jet just north of the equator (Fig. 4(a)). On 13 January, the day of monsoon onset, the centre of this anticyclone was entirely north of Australia as a short-wave trough in the subtropical westerlies lowered 200 mb heights over the continent; this accounts for the upper westerlies in Fig. 2. The reason for the displacement of the mean tropical easterly jet north of the equator can be seen in Fig. 4(b): a mean zonal gradient of geopotential on the equator associated with a very-large-scale height pattern, with higher heights over the Pacific than over the Indian ocean. This pattern is climatological, and can also be seen, for example, in Ramage (1971, Fig. 7.4). With the twin maxima, somewhat symmetric across the equator, it bears some resemblance to an equatorially trapped planetary wave, and hence to Gill's (1980) simple solutions for heat-induced tropical flow.

Figure 5 shows the percentage high cloudiness (PHC) from 168 3-hourly infrared satellite images for the period 00 GMT 14 January–00 GMT 4 February 1987 (same period as Figs. 3 and 4). High cloudiness is defined by equivalent black-body temperatures less than 218 K (−55 °C), corresponding to the 200 mb level. This threshold is arbitrary, but it outlines MCSs reasonably well (individual pictures, enhanced at the −55 °C level, are

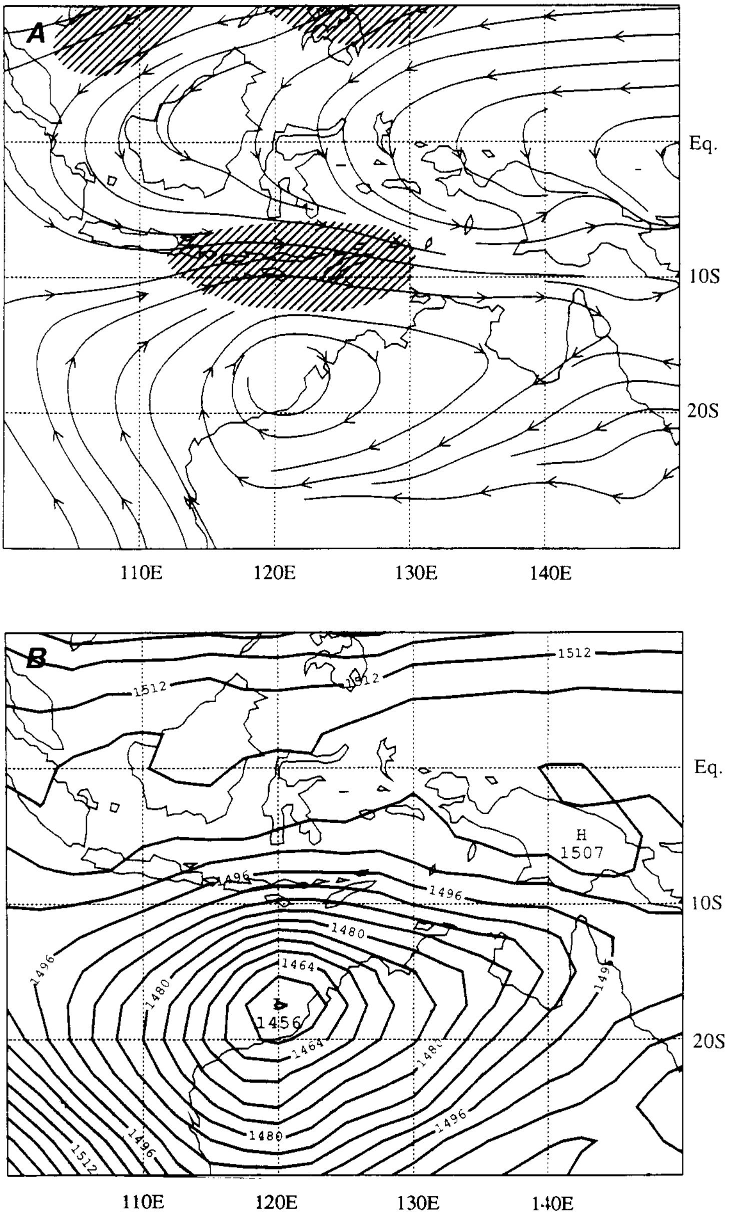

Figure 3. Mean 850 mb fields from ECMWF 12 GMT analyses for the three-week period 14 January to 3 February 1987 that contained the ten EMEX flight missions. (a) Streamlines and isotachs. Hatched areas: wind speed > 10 m s^{-1}. (b) Geopotential height.

in section 5). The PHC presentation of satellite data was chosen for its approximate relation to rainfall (Janowiak and Arkin 1991).

Figure 5 indicates that most of the precipitating convection in the Australian longitudes occurred south of the equator, over the ocean, but near the coast. A similar offshore enhancement of Indian monsoon cloudiness has been extensively studied (Ogura and Yoshizaki 1988 and refs.), though it is poorly documented. There was a small maximum in PHC in the Australian Low (120°E, 18°S), corresponding to the cold tops

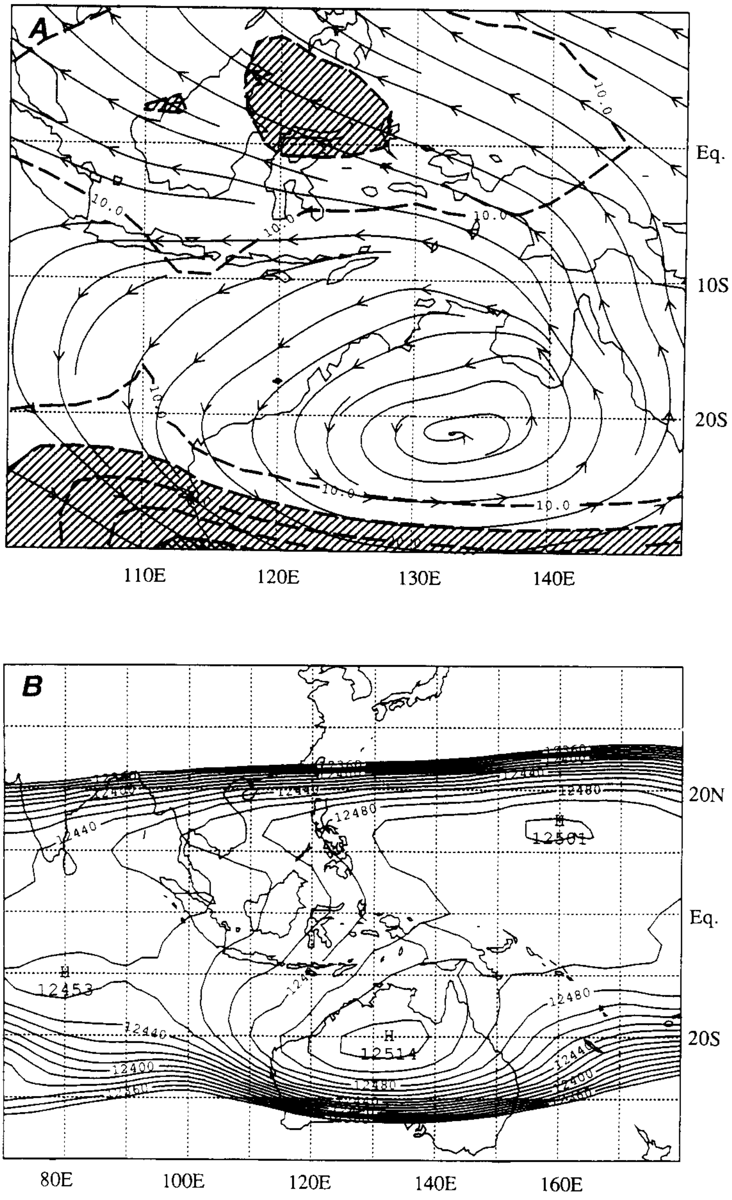

Figure 4. As Fig. 3, except at 200 mb. In (a) hatched areas: wind speed > 15 m s^{-1}.

of cyclones Connie and Damien, while a much larger area of cold cloudiness showed up wrapped around the north Australian coast, north and west of the 'Top End' peninsula. A third small maximum can be seen in the Java Sea south-east of Borneo (117°E, 7°S).

(*b*) *Vorticity considerations*

In understanding the effects of convection on the synoptic-scale flow, it is useful to refer to the equation governing the vertical component of vorticity calculated from

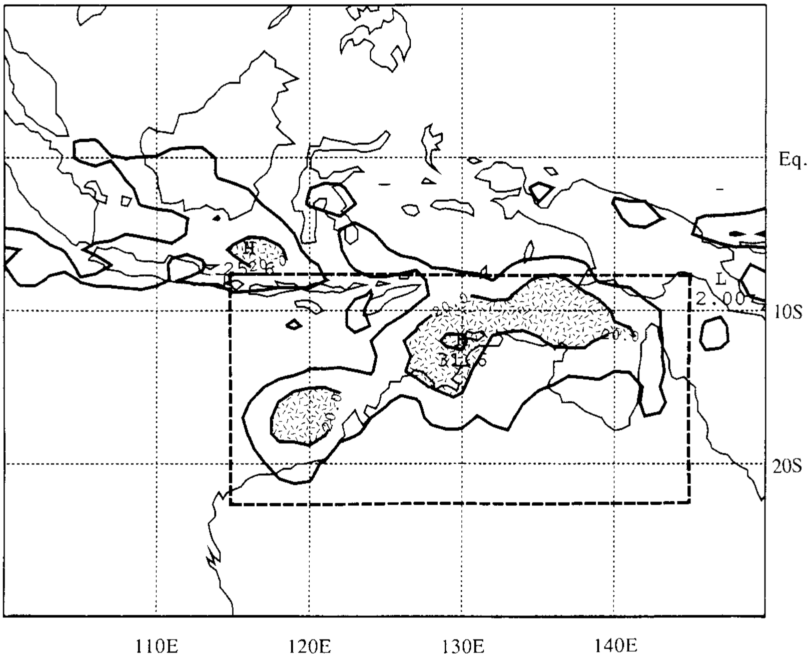

Figure 5. Percentage high cloudiness, defined as the percentage of 3-hourly infrared satellite images in which the equivalent black-body temperature was colder than −55 °C, during the time interval 14 January to 3 February 1987. Contour interval 10%, stippling above 20%.

synoptic-scale wind fields (viz the ECMWF-analysed winds). Vorticity budgets for regions containing tropical cloud systems have been calculated by other authors (e.g. Sui and Yanai 1986), and theories have been suggested for parametrizing cloud effects on large-scale vorticity (e.g. Cho *et al.* 1979). But as pointed out by Esbensen *et al.* (1987) and by Haynes and McIntyre (1987, 1990), vorticity has important conservation properties that can be obscured by the expansion of cloud effects into multiple terms, and can be lost entirely in schemes that evaluate or parametrize those terms independently.

In the spirit of the latter authors, a simple, yet complete, vorticity equation can be derived from the momentum equation governing a hydrostatic, pressure-coordinate synoptic-scale representation ($\mathbf{U}$, ω) of an actual flow field, $\mathbf{U}$ being the horizontal wind vector (u, v, 0), and ω the rate of change of pressure following a parcel of air. The ECMWF analyses, on a 2·5° grid, would constitute such a representation, if they were perfect. The horizontal momentum equation is:

$$\frac{\partial \mathbf{U}}{\partial t} + \mathbf{U} \cdot \nabla \mathbf{U} + \omega \frac{\partial \mathbf{U}}{\partial p} = -f\hat{\mathbf{k}} \times \mathbf{U} - \nabla \Phi + \mathbf{F} \qquad (1)$$

where t is time, p is pressure, $\hat{\mathbf{k}}$ is the vertical unit vector, f is the Coriolis parameter, Φ is geopotential, and $\mathbf{F}$ is the residual or apparent acceleration on the resolved scale resulting from all sub-resolvable sources of momentum, including horizontal and vertical transports and non-hydrostatic pressure-gradient forces. In the case of tropical synoptic-scale momentum studies, $\mathbf{F}$ is typically assumed to be dominated by the vertical transport of momentum in convective systems.

Now after taking the vertical component of the pressure-coordinate curl of (1), an equation for the vorticity of the resolved flow is obtained:

$$\begin{aligned}\frac{\mathrm{D}\zeta_\mathrm{a}}{\mathrm{D}t} &\equiv \left(\frac{\partial}{\partial t} + \mathbf{U}\cdot\nabla_p\right)\zeta_\mathrm{a} \\ &= \frac{\mathrm{D}\zeta}{\mathrm{D}t} + \beta v \\ &= -\zeta_\mathrm{a}(\nabla_p\cdot\mathbf{U}) - \hat{\mathbf{k}}\cdot\nabla_p\times\left(\omega\frac{\partial\mathbf{U}}{\partial p} - \mathbf{F}\right) \qquad (2)\end{aligned}$$

where $\nabla_p \equiv \left(\frac{\partial}{\partial x}, \frac{\partial}{\partial y}, \frac{\partial}{\partial p}\right)$, $\zeta = \hat{\mathbf{k}}\cdot\nabla_p\times\mathbf{U}$ is the vertical component of relative vorticity, ζ_a is the absolute vorticity $f + \zeta$, β is $\partial f/\partial y$, and v is the meridional component of $\mathbf{U}$.

The first term on the right, often called 'vortex stretching', acts to increase the magnitude of absolute vorticity of either sign in the presence of convergence, and to decrease it in the presence of divergence. The *net* mass sink at low levels and mass source at upper levels associated with the net heating in precipitation systems will be reflected in the divergence of the resolved-scale winds, even if the flow on the scale of the precipitation systems is not resolved *per se*. This is not to say that the ECMWF-analysed fields contain the correct divergent winds; they do not. However, the actual divergence patterns, which can be qualitatively inferred from the satellite-observed population of cloud systems, do help explain the evolution of the vorticity, and thus of the rotational winds, which, being of much larger magnitude, are probably more accurately represented in the ECMWF analyses. This interplay of the rotational and divergent winds has been exploited, for example, by Sardeshmukh and Hoskins (1987) in their 'χ-problem' calculation of accurate global 200 mb divergent wind fields from the evolution of the ECMWF-analysed rotational winds.

The second term on the right-hand side (RHS) of (2) is the curl of the apparent acceleration resulting from the total vertical advection of momentum, 'mean' plus 'eddy' (plus all other neglected accelerations). The eddy and mean separation is arbitrary and resolution-dependent, so any further expansion of the force-curl term would be purely a mathematical exercise, which might obscure the conservation properties inherent in the curl form.

Since vertical velocity and, therefore, divergence are small in the tropics in the absence of diabatic heating (e.g. Charney 1963), the first term on the RHS of (2) will be concentrated in areas of precipitation, where in general net low-level convergence and upper-level divergence prevail (the detailed vertical structure of this divergence will be the subject of Part II). If, in addition, the subgrid-scale momentum source **F** is dominated by vertical transports within MCSs, the acceleration vector (in parentheses) in the second term on the RHS of (2) is, like divergence, localized in areas of MCS activity. Hence, the curl of this patchy vector field should be manifest in the appearance of vorticity couplets flanking cloudy areas, positive to the left and negative to the right of **F**. Such vorticity couplets flanking MCSs have been reported in the eastern Atlantic (Tollerud and Esbensen 1983; Sui and Yanai 1986).

The fields of mean absolute vorticity corresponding to Figs. 3(a) and 4(a) are shown in Figs. 6(a) and (b). In these plots, the units of absolute vorticity are degrees latitude, corresponding to the 'rest latitude' at which the planetary vorticity is equal to the given value of absolute vorticity. This convention makes explicit the idea that absolute vorticity can be used as a tracer of meridional displacements, with the proviso that the terms on the RHS of (2) will modify it, mostly in convectively active areas and in the frictional boundary layer. In this context it is useful to note that divergence can never change the

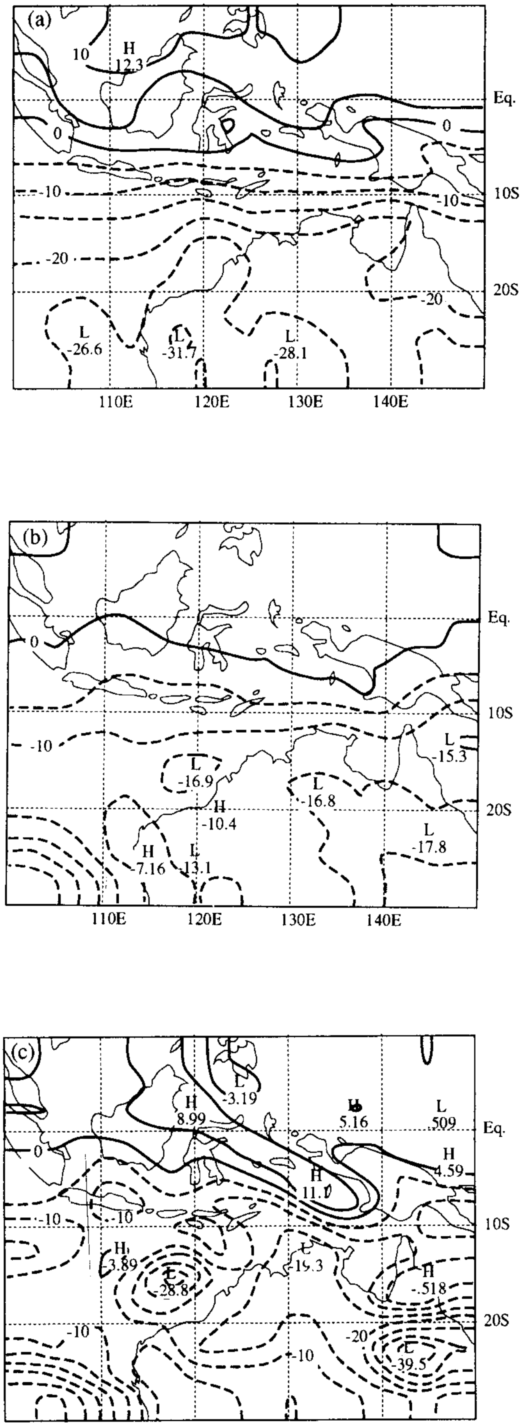

Figure 6. Mean values of absolute vorticity derived from ECMWF analyses, in 'rest latitude' units (the latitude in degrees at which the planetary vorticity has the given value). Contour interval 5 degrees. (a) At 850 mb, mean for the period 14 January–3 February. (b) At 200 mb, mean for the period 14 January–3 February. (c) At 200 mb, mean for the period 1–3 February.

sign of absolute vorticity, only its magnitude. Friction, if it is assumed to oppose the wind, will tend to bring the relative vorticity to zero, such that the absolute-vorticity contours relax back toward their rest latitudes.

It is instructive to examine the time-mean vorticity fields of Fig. 6 for evidence of (i) the mean 850 mb mass sink/200 mb mass source implied by Fig. 5; (ii) the mean meridional flows in Figs. 3(a) and 4(a); and (iii) momentum fluxes by convection. In addition, transient eddy fluxes of vorticity must also be considered.

The mean vorticity pattern at 850 mb, corresponding to the winds in Fig. 3(a), is shown in Fig. 6(a). The contour of zero absolute vorticity lies roughly 5° south of the equator, because the relative vorticity north of there is positive. This positive vorticity was evidently advected in from the northern hemisphere by the persistent mean northerly winds across the equator. To the south of the zonal jet at 10°S, contours tended to lie equatorward of their rest latitudes, indicating cyclonic relative vorticity. Cyclonic (negative) vorticity in these areas was locally increased by the low-level convergence associated with the convective systems along the Australian coast, as well as advected from the south by the mean southerlies in western Australia and the eastern Indian Ocean (not as persistent as the cross-equatorial northerlies). Transient eddy fluxes of vorticity removed cyclonic vorticity from the time-mean trough, as hurricanes formed in the trough and then moved out during the averaging period.

The 200 mb pattern of mean absolute vorticity, corresponding to the winds in Fig. 4(a), is shown in Fig. 6(b). At this level, divergence from the convective systems near the Australian coast acted to lessen any vorticity of either sign, and this outflow air with near-zero vorticity flowed north-westward across the equator at all longitudes, and southward over western Australia. Hence, the vorticity field in Fig. 6(b) shows very small absolute vorticity near, and north of, the equator and in western Australia. In the southern hemisphere almost all the contours lie poleward of their rest latitudes, indicating anticyclonic relative vorticity.

One particular notable feature is the area of positive absolute vorticity south of the equator (0–8°S), north of the PHC maximum, from 130–140°E. Since divergence can never change the sign of absolute vorticity, and the mean meridional wind in this area was southerly, reference to (2) suggests that this feature must reflect a subgrid-scale source of momentum, presumably a vertical transfer by convective systems. In fact, this feature was very pronounced from 1–3 February (Fig. 6(c)), when persistent, well-sampled (EMEX flights 8, 9, 10) MCSs in the Arafura Sea (10°S, 135°E on Fig. 8(e)) were observed to be transporting westerly momentum upward.

(*c*) *Time progression*

The five three-day time periods discussed in this section were chosen to represent the various synoptic regimes within which the EMEX convective systems were observed. They are denoted *onset* (14–16 January; EMEX flights 1, 2, 3), *cyclones* (18–20 January; EMEX flights 4, 5), *inactive* (23–25 January; no flights), *second onset* (27–29 January; EMEX flights 6, 7), and *long zonal fetch* (1–3 February; EMEX flights 8, 9, 10). High cloudiness and 700 mb wind maps for these periods are shown in Figs. 7 and 8.

The *onset* convection occurred primarily in the Bonaparte Gulf (12°S, 129°E in Fig. 7(a)) over the earth's warmest January-mean sea surface temperature (30 °C, Fig. 9). The Australian Low, with cyclone Connie in its centre, quickly spun up (Fig. 8(a)). Cyclone Irma developed in the Gulf of Carpentaria, and in the *cyclones* period most high cloudiness was associated with the two cyclones (Figs. 7(b) and 8(b)). After the westward and poleward motion of the cyclones, to their demises, the *inactive* period ensued (Figs. 7(c) and 8(c)). The Bonaparte Gulf was again the site of the resurgence

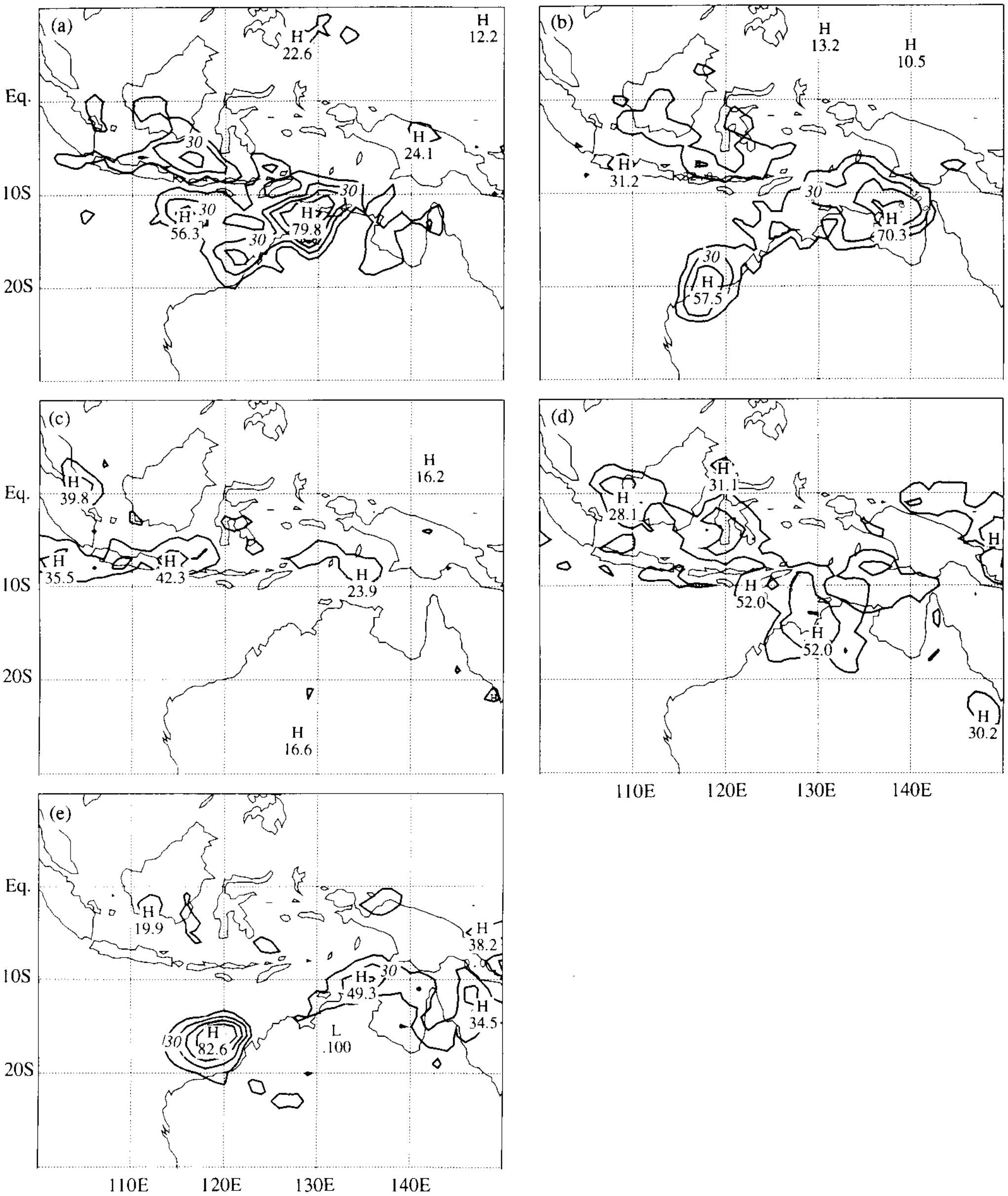

Figure 7. Percentage high cloudiness (defined in Fig. 5) for five three-day periods: (a) *onset*, 14–16 January; (b) *cyclones*, 18–20 January; (c) *inactive*, 23–25 January; (d) *second onset*, 27–29 January; (e) *long zonal fetch*, 1–3 February.

of convection during the *second onset*, as the Australian Low depression, soon to contain cyclone Damien, developed in that region (12°S, 130°E in Figs. 7(d) and 8(d)). During *long zonal fetch*, strong monsoon westerlies spanned the entire Australian continent, and in addition to Damien's cloudiness, a second convective maximum appeared in the Arafura Sea (10°S, 135°E in Figs. 7(e) and 8(e)). After the final EMEX aircraft missions were flown in that area, cyclone Jason occurred in the Gulf of Carpentaria, and a two-cyclone pattern not unlike Fig. 8(b) prevailed again, until the cyclones again moved into unfavourable environments.

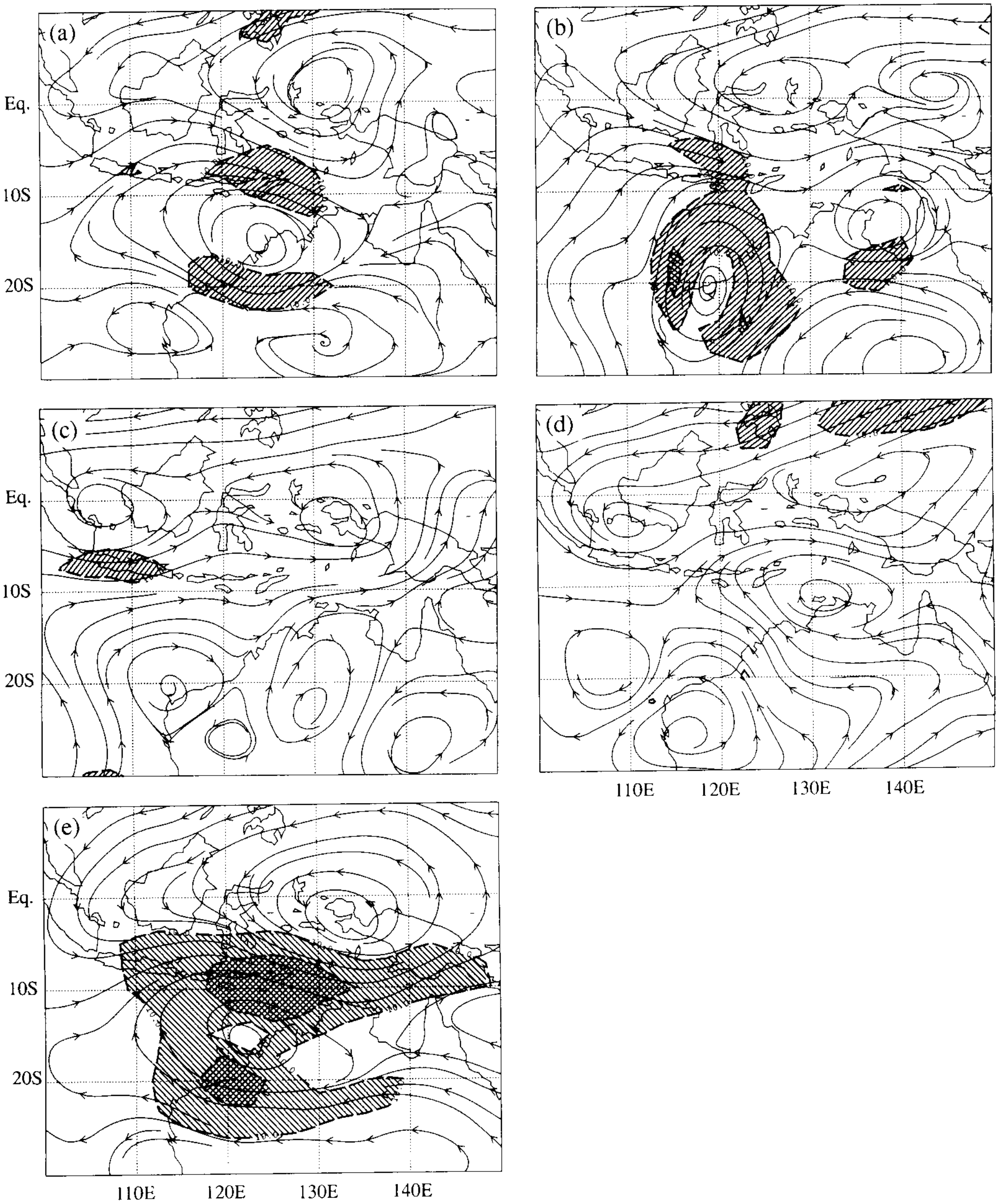

Figure 8. Streamlines and isotachs at 700 mb, from ECMWF 12 GMT analyses, for the periods defined in Fig. 7. Isotachs shown at 10 m s^{-1} (hatched) and 15 m s^{-1} (cross-hatched).

4. THERMODYNAMIC CONDITIONS FOR BUOYANT CONVECTION

In this section we address the second major issue of this study, namely the energy supply for the widespread, persistent, deep convection which characterizes the monsoon and spins up its cyclones. Since tropical deep convection is based on the boundary layer, it is traditional to assess the viability of convection on the basis of the buoyancy of unmixed updraught parcels of boundary-layer air. While downdraughts are an important part of MCSs, the bulk of convective energy comes from buoyant updraughts, the *sine*

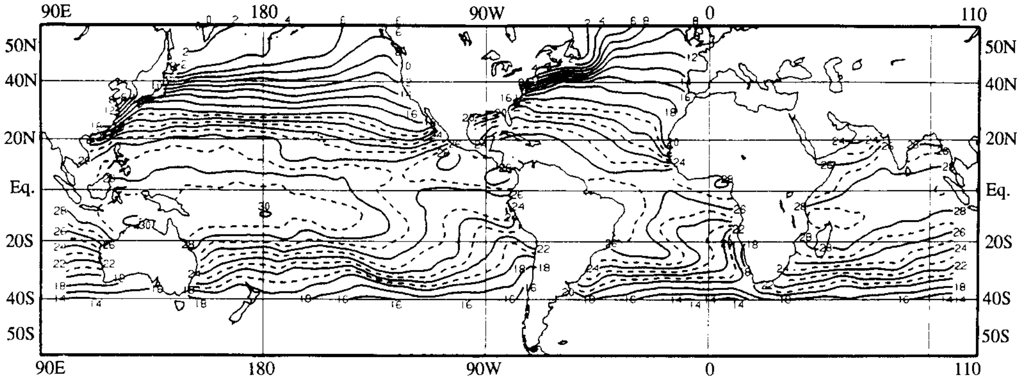

Figure 9. January 1987 mean sea surface temperature map, from the U.S. NOAA Climate Analysis Center's Climate Diagnostics Bulletin.

qua non of deep convection. Real updraughts undergo entrainment, but the arbitrary parameters introduced in attempts to quantify it (see for example Betts 1974) would add more uncertainty and clutter than insight to this discussion.

The AMEX soundings used in this section differed little from one another, as is typical of tropical soundings (Betts 1974; Aspliden 1976; Xu and Emanuel 1989). For this reason we express individual soundings as deviations from a reference sounding (Fig. 10), the mean of all AMEX Phase II soundings (4 times daily, 13 January to 14 February) from the EMEX ship *Xiang Yang Hong No.* 5 at 11°S, 139°E (see Fig. 1).

(*a*) *Buoyancy and CAPE*

A useful energetic measure of the viability of convection is convective available potential energy (or 'positive area' on a thermodynamic chart), defined as the integral over height of the upward buoyancy acceleration, B, felt by a parcel rising pseudo-adiabatically from its level of free convection (LFC) to its level of neutral buoyancy (LNB):

$$\mathrm{CAPE} = \int_{\mathrm{LFC}}^{\mathrm{LNB}} B\,\mathrm{d}z. \tag{3}$$

The integrand and limits of integration, and therefore CAPE, depend only on the parcel's equivalent potential temperature, θ_e, (in graphical terms, the moist adiabat along which it ascends) and on the ambient density profile through which it is assumed to rise.

(i) *Boundary-layer* θ_e. CAPE is a parcel property (units J kg^{-1}), and is very sensitive to the θ_e of the arbitrarily defined parcel. Moreover, θ_e varies on small horizontal and vertical scales in the monsoon boundary layer (apparent from aircraft data). As a result, CAPE calculated from an individual sounding, whatever the choice of parcel, will generally have little bearing on the likelihood or intensity of convection a few hundred kilometres away or a few hours later.

Figure 11 shows profiles of buoyancy, relative to the ship-mean reference sounding, for parcels with specified values of θ_e, lifted pseudo-adiabatically (liquid water assumed to fall out instantly as it condenses) and reversibly (all liquid water retained, but with its small heat capacity neglected). Aircraft measurements of liquid water in deep convection indicate that nature is closer to the pseudo-adiabatic idealization than to the reversible. The area under each curve is proportional to CAPE in this figure; for reference, the 350, 355, and 360 K parcels, rising adiabatically, have CAPE values of 260, 1180, and

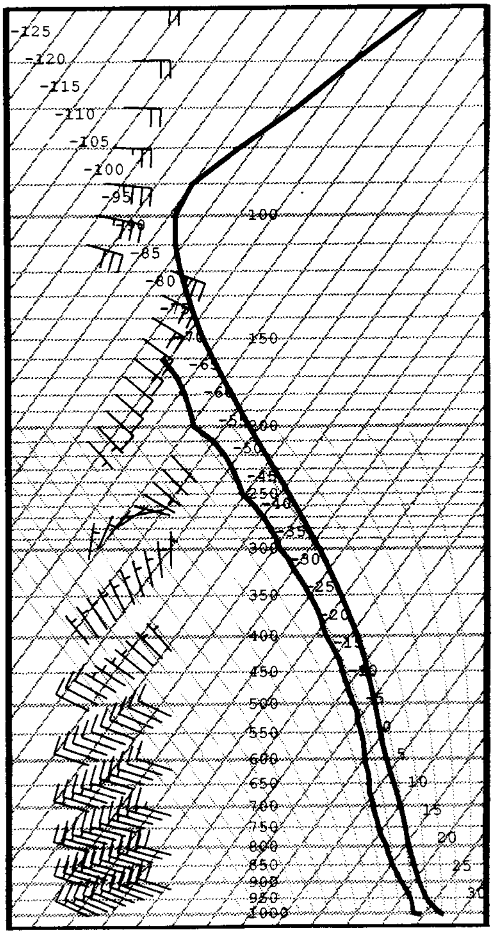

Figure 10. Mean of all AMEX Phase II (4 per day, 13 January–15 February 1987) soundings from the Chinese ship at 11°S, 139·5°E. Skew-T, log-p format.

2370 J kg^{-1}, respectively. Inclusion of the neglected latent heat of freezing would increase these values slightly. Parcels have positive buoyancy, and therefore upward acceleration, throughout the troposphere. If entrainment and drag forces are weak, the altitude of the maximum convective updraught velocities can be quite high (see section 5(a)). The area to the right of the 340 K curve in Fig. 11 indicates the energy available to accelerate a saturated downdraught with that value of θ_e.

The sensitivity of CAPE to parcel temperature (T), relative humidity (RH), and pressure can be quantified as follows. Writing the functional dependence of CAPE as CAPE (sounding, parcel $\theta_e(T, \text{RH}, p)$), and evaluating derivatives at a typical Australian monsoon boundary-layer value ($T = 28\,°\text{C}$, $\text{RH} = 75\%$, $p = 1000$ mb, with $\theta_e = 355$ K), yields:

$$\frac{\partial \text{CAPE}}{\partial T} = \frac{\partial \text{CAPE}}{\partial \theta_e} \cdot \left.\frac{\partial \theta_e}{\partial T}\right]_{\text{RH},p} \approx \frac{1100\ \text{J kg}^{-1}}{5\ \text{K}} \cdot \frac{5\ \text{K}}{1\ \text{deg C}} \approx \frac{1000\ \text{J kg}^{-1}}{1\ \text{deg C}} \tag{4a}$$

$$\frac{\partial \text{CAPE}}{\partial \text{RH}} = \frac{\partial \text{CAPE}}{\partial \theta_e} \cdot \left.\frac{\partial \theta_e}{\partial \text{RH}}\right]_{T,p} \approx \frac{1100\ \text{J kg}^{-1}}{5\ \text{K}} \cdot \frac{8\ \text{K}}{10\%} \approx \frac{1000\ \text{J kg}^{-1}}{6\%} \tag{4b}$$

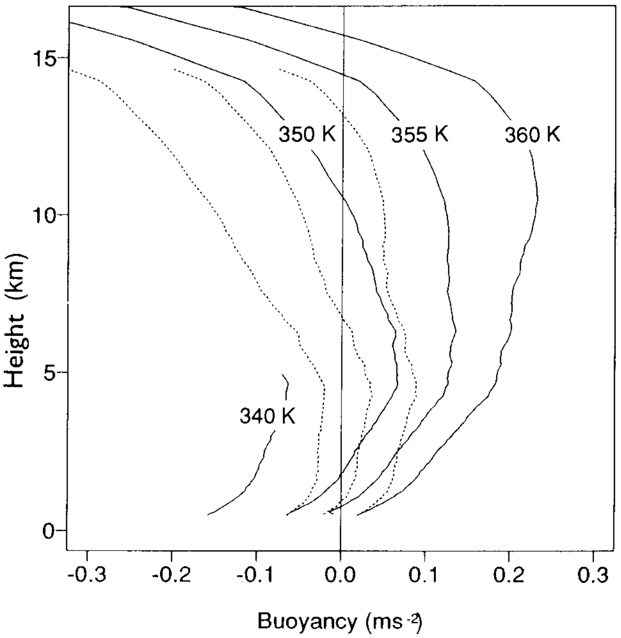

Figure 11. Buoyancy of saturated parcels with the indicated values of equivalent potential temperature, relative to the ship mean sounding (Fig. 10). Solid lines: pseudo-adiabatic ascent; dashed lines: reversible ascent (all liquid water retained). CAPE is the area under the curves.

$$\frac{\partial \mathrm{CAPE}}{\partial p} = \frac{\partial \mathrm{CAPE}}{\partial \theta_\mathrm{e}} \cdot \left.\frac{\partial \theta_\mathrm{e}}{\partial p}\right]_{T,\mathrm{RH}} \approx \frac{1100\,\mathrm{J\,kg^{-1}}}{5\,\mathrm{K}} \cdot \frac{5\,\mathrm{K}}{-31\,\mathrm{mb}} \approx \frac{1000\,\mathrm{J\,kg^{-1}}}{-28\,\mathrm{mb}}. \tag{4c}$$

The large magnitudes of these sensitivities illustrate the basis for Xu and Emanuel's (1989) exhortation that processes affecting subcloud-layer moist entropy (or θ_e) be considered when evaluating the energy supply of convectively driven tropical circulations. Note that humidity measurement errors are quite substantial in terms of CAPE.

Although (4) are in terms of *convective* available potential energy, they are valid for any circulation system drawing its energy from saturated ascent. One example is Emanuel's (1986) idealized mature hurricane, in which ascent in the eyewall is slantwise neutral (CAPE is zero), owing to the very warm environment, and the energy goes directly into the cyclone-scale circulation rather than into the kinetic energy of convective turbulence.

Maximum values of θ_e observed in the boundary layers feeding into the EMEX convection, as observed by the F27 and Electra aircraft, were 355 to 360 K. The absolute maximum aircraft-observed value of θ_e was 364 K, measured by the F27 at very low altitude on 23 January, during suppressed conditions. Dropwindsondes routinely reported values over 370 K, but their moisture sensors are known to over-estimate (e.g. Powell 1990b). Figure 12 shows a climatology of boundary-layer θ_e in the *Xiang Yang Hong No. 5* soundings, with θ_e converted to CAPE using the linearized formula (from Fig. 11) CAPE $= 260 + 211(\theta_\mathrm{e} - 350)$. Generally, CAPE decreased monotonically with height, reflecting the fact that the subcloud 'mixed layer', while well mixed in terms of potential density, is typically not well mixed in terms of water vapour (Xu and Emanuel 1989). Mean values (curve m) decreased from about 1000 J kg^{-1} at the surface to near 0 at

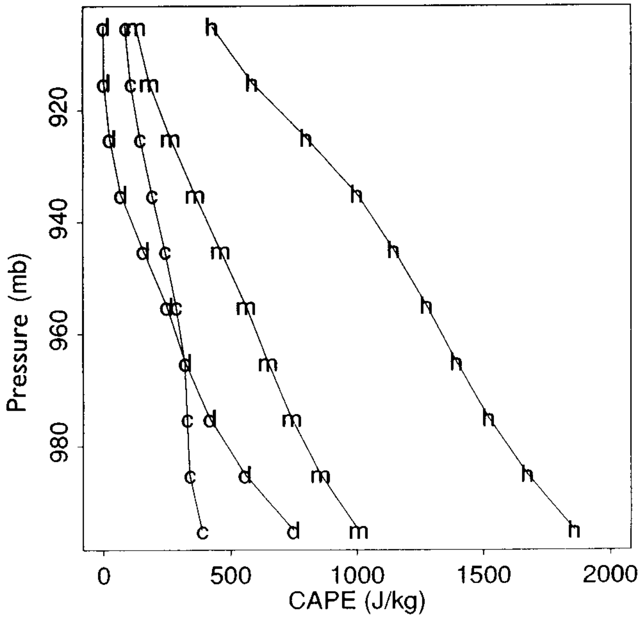

Figure 12. CAPE (linearized function of θ_e, see text) as a function of pressure in the boundary layer, from soundings at the ship (11°S, 139°E). The curves represent mean soundings: m, the mean of all 130 soundings; h, the mean of the quartile of the soundings with the greatest integrated CAPE; d, the mean of the quartile with the greatest dew-point depression at 920 mb; c, the mean of the quartile with the lowest surface air temperature ($T_s < 26.8$ °C).

900 mb, while the mean of the quartile of the soundings with the highest integrated CAPE (curve h) had CAPE values approximately twice as large at all levels. Cold penetrative downdraughts in convection (curve c), and dry subsidence (curve d), led to reduced values of CAPE.

(ii) *Deep tropospheric sounding variability.* A consistent, though small, synoptic modulation of CAPE was associated with changes in the deep tropospheric temperature structure. These changes in the CAPE experienced by parcels *with a given value* of θ_e can also be represented as areas on a buoyancy–height diagram, with virtual temperature deviations (at constant pressure) expressed as buoyancy, relative to the ship-mean reference sounding.

Figure 13 shows composite daily-mean virtual temperature perturbations in six categories, determined according to satellite-observed daily PHC in the vicinity of each of the five northernmost coastal sounding sites. Category 6, with PHC exceeding 40%, is composed of soundings near named tropical cyclones, plus some Darwin soundings from the *onset* period (Fig. 7(a)), while the soundings of category 1 come largely from the *inactive* period (Fig. 7(c)). The peak-to-peak composite upper-tropospheric buoyancy variation was approximately 0.1 m s^{-2}, corresponding to a virtual temperature variation of about 2 deg C.

Three major features are apparent in Fig. 13. First, the deep upper-tropospheric warming from 5–14 km or so makes CAPE, for a given parcel θ_e, *decrease* by 280 J kg^{-1} (the area between curves 1 and 6) during convectively active periods. Second, the curves cross at 14 km, indicating cooling aloft during active convective periods. This may reflect a higher mean tropopause, or possibly the mesoscale cold lenses above individual tropical MCSs, as reported by Johnson and Kriete (1982, their Fig. 3(a)) and analytically

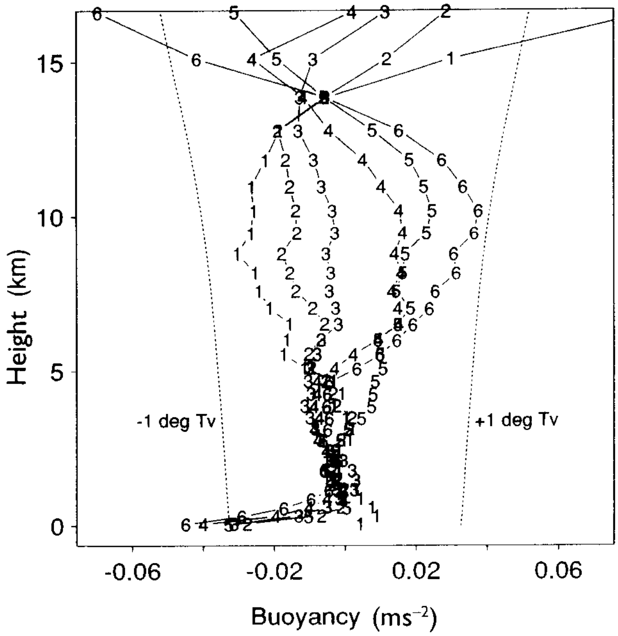

Figure 13. Percentage-high-cloudiness composite daily-mean soundings from the five AMEX sites north of 15°S (see Fig. 1). Plotted are virtual-temperature deviations from the ship-mean sounding, expressed as buoyancy. The composite categories, defined in terms of daily percentage high cloudiness in square areas 400 km on a side centred on the sounding sites, are (with number of daily-mean soundings in each category in parentheses): category 1: 0–5% (29); 2: 5–10% (29); 3: 10–20% (38); 4: 20–30% (29); 5: 30–40% (11); 6: >40% (18).

reproduced by Nicholls *et al.* (1991, their Fig. 6(d)). Third, the boundary layer tends to be cooler in the mean during active (cloudy) periods, owing to the large area covered by disturbed (cold) boundary-layer air, typically 30% in GATE for example (Gaynor and Ropelewski 1979). This observation does not necessarily imply that the boundary-layer air *feeding into the deep convection* is cooler during more active periods.

In addition, cooler air does not necessarily have lower θ_e. The disturbed (cold) boundary layer includes ambient subcloud-layer air cooled by the evaporation of light rain (with increased humidity but unchanged θ_e), as well as the low-θ_e cold air from downdraughts in heavier rain areas (Barnes and Garstang 1982). In fact, the boundary-layer θ_e profiles of the six composite mean soundings are essentially indistinguishable (not shown), except for the higher θ_e during the suppressed conditions of category 1. When MCSs do form in such 'break monsoon' conditions, they are vigorous and highly electrified (Rutledge *et al.* 1992).

(*b*) *Forcing, triggering and feedbacks*: *controls on the incidence of convection*

The above observations indicate that more deep convection occurs when CAPE is lower. A similar condition characterizes easterly waves (Reed and Recker 1971; Thompson *et al.* 1979). Hence, while the vertical velocity in synoptic-scale areas containing convection has an upward *mean* value through the troposphere, the convection is apparently not caused by *large-scale* deep upward motions destabilizing the troposphere. Instead, low-level processes, including the frequency of small-scale intense lifting events necessary to trigger convection, as well as larger-scale processes like adiabatic mass convergence, are apparently responsible for the modulation of convection. Low-level convergence favours convection in two ways: it increases the depth of the high-θ_e layer near the surface, and it adiabatically cools the ambient air, which lowers the LFC of ascending parcels and thereby decreases the convective inhibition or 'negative area' on a thermodynamic chart. Which of these mechanisms predominates over the warm tropical ocean is unknown. A high vertical-resolution sounding data set, like the AMEX data set but with detailed information on the local conditions sampled by the sondes, could shed light on this important question.

Many of the low-level processes modulating convection act as positive feedbacks. In other words, convection is favoured by previous convection. The sharpness of monsoon onset, and the substantial interannual variability in its date (Holland 1986) support the notion that the monsoon is an unstable positive-feedback process, waiting for a trigger, once the seasonal conditions are ripe (e.g. the warm water is in place). Disturbances which may trigger monsoon onset include the intraseasonal (40–50 day) oscillation (Hendon and Liebmann 1990) and mid-latitude disturbances (e.g. Keenan and Brody 1988, upper westerlies in Fig. 2). Active sub-periods within a monsoon season also tend to persist once they begin.

The high degree of overlap and interconnectedness of monsoon MCSs can be objectively demonstrated from infrared (IR) satellite data. Consider the following definition of a 'cloud cluster', from Williams and Houze (1987). A 'cluster element' is a spatially connected area (at 10 km resolution), of at least moderate size ($>5000\,\mathrm{km}^2$), with black-body temperature colder than −65 °C (Williams and Houze used −60 °C) in an IR satellite image. A cloud cluster is a set of temporally connected cluster elements, where two cluster elements are said to be part of the same cloud cluster if their spatial overlap from one image to the next (3 h intervals) exceeds half the size of either cluster element or $10000\,\mathrm{km}^2$. By the above definition most of the monsoon convection from 14 to 21 January 1987, including both cyclones Connie and Irma, constituted *a single giant cloud cluster*. Other Australian monsoon 'superclusters' extended from 31 January to 4 February and from 5 to 9 February (see Fig. 7 of Mapes 1992a). Monsoon convection, once triggered, lasted until hurricanes formed and eventually died of the usual causes (landfall or poleward drift).

What are the mechanisms of positive feedback? An obvious one is that convective downdraughts form a surface cold pool, which triggers further convection by lifting adjacent high-θ_e boundary-layer air. As emphasized by Houze and Betts (1981), this mechanism is so efficient that MCSs, rather than individual cumulonimbus clouds, are the basic unit of tropical precipitation. While the cold air suppresses deep convection locally, surface fluxes restore the boundary layer to a state of convective readiness in about half a day (Houze 1977; Zipser 1977; Fitzjarrald and Garstang 1981; Nicholls and Johnson 1984; Powell 1990b), so twice-daily overturning could theoretically be sustained even in the absence of horizontal advection, as long as the oceanic heat source lasts. Other feedback mechanisms, detailed below, can be divided into two types: thermodynamic and dynamical.

One thermodynamic feedback is the humidification of the deep troposphere by initial convection, which can create more favourable conditions for the growth of later convective cells, as found by Dudhia and Moncrieff (1987) in a modelling study of a GATE MCS. Another is the wind-evaporation feedback, in which enhanced surface moisture fluxes result from the surface winds associated with convectively driven circulations. Heat flux from the ocean is dominated by latent-heat flux, which is primarily sensitive to wind speed (e.g. Aspliden 1976). Wind-evaporation feedback is well known in the case of hurricanes, has been shown to be of some importance to the intraseasonal oscillation (Emanuel 1987; Neelin *et al.* 1987), and may have global significance. For example, in a zonally symmetric model, the same amount of atmospheric heating causes much greater globally integrated surface winds if it is a few degrees off the equator than if it is on the equator (Lindzen and Hou 1988).

Another thermodynamic feedback important in hurricanes is the pressure–evaporation feedback. If surface fluxes maintain the temperature and relative humidity of boundary-layer air as it spirals into the low-pressure centre, it arrives at the hurricane eyewall with dramatically increased θ_e. As a result, hurricanes can persist even in environments with no ambient CAPE (Emanuel 1986).

Hurricane secondary circulation is a well-known example of a dynamical positive feedback. Any surface pressure minimum is necessarily surrounded by a divergent pressure gradient, which causes convergence of the frictional cross-isobaric component of flow in the boundary layer. This convergence leads to convection, which further strengthens the cyclone and its surface pressure field, and so on. This positive-feedback mechanism was denoted CISK (Conditional Instability of the Second Kind) by Charney and Eliassen (1964).

An inviscid, nonrotating version of CISK also exists for heating with a profile shaped like that observed in Australian monsoon MCSs (Mapes 1992a). This fact may seem surprising, as convection has often been assumed to suppress additional convection in its vicinity by means of its 'compensating subsidence' field. But the environmental state induced by MCS heating in fact consists, at low levels, of a large remote area in which 'overcompensating subsidence' has depressed material surfaces, and a smaller region near the MCS in which inviscid ascent has lifted material surfaces above their undisturbed levels. Convection is therefore favoured in the region near previous convection, so this mechanism constitutes another dynamical positive feedback.

Observations suggest that *all* of these positive feebacks—increased cold-pool frequency, tropospheric moistening, wind-enhanced evaporation, pressure-enhanced evaporation in the cyclone cores, and dynamical lifting—are active in the Australian monsoon. An implication of this is that even bulk measures like seasonal monsoon precipitation amount may depend, as monsoon onset timing certainly does, on hard-to-predict triggering disturbances.

(*c*) *The effect of convection on the environment: heating vs spin-up*

It is curious that the deep upper-tropospheric temperature variation, shown by Fig. 13 to be positively correlated with PHC, and therefore with precipitation and latent-heating rate, is hydrostatically related almost entirely to *low-level* pressure variations (Fig. 14(a)). If the observed increase in temperature with PHC were due to a local build-up of the heat from the increased latent-heating rate, one might expect it to be associated also with an increase in upper-tropospheric pressure or geopotential height. A further clue is provided by Fig. 14(b), which indicates that PHC is systematically related to cyclonic vorticity through a deep layer of the lower troposphere. (The relationship between Figs. 14(a) and (b) is only heuristic, since the vorticity measurements of Fig. 14(b) are an area-average over the Gulf of Carpentaria.)

It appears that the observed temperature increase is hypsometrically related to low surface pressure accompanying the low-level cyclonic circulation, which happens to be associated with increased PHC (for reasons explored above). The higher temperatures are not an indication of the increased instantaneous latent-heating rate. In other words, the monsoon thermal structure is dynamically related to the wind fields in the thermal wind sense, similar to the thermal structure of easterly waves (Cho and Jenkins 1987). The temperature increase is only indirectly related to heating, in that the monsoon cyclonic vorticity is due mainly (through the first term on the RHS of (2)) to a history

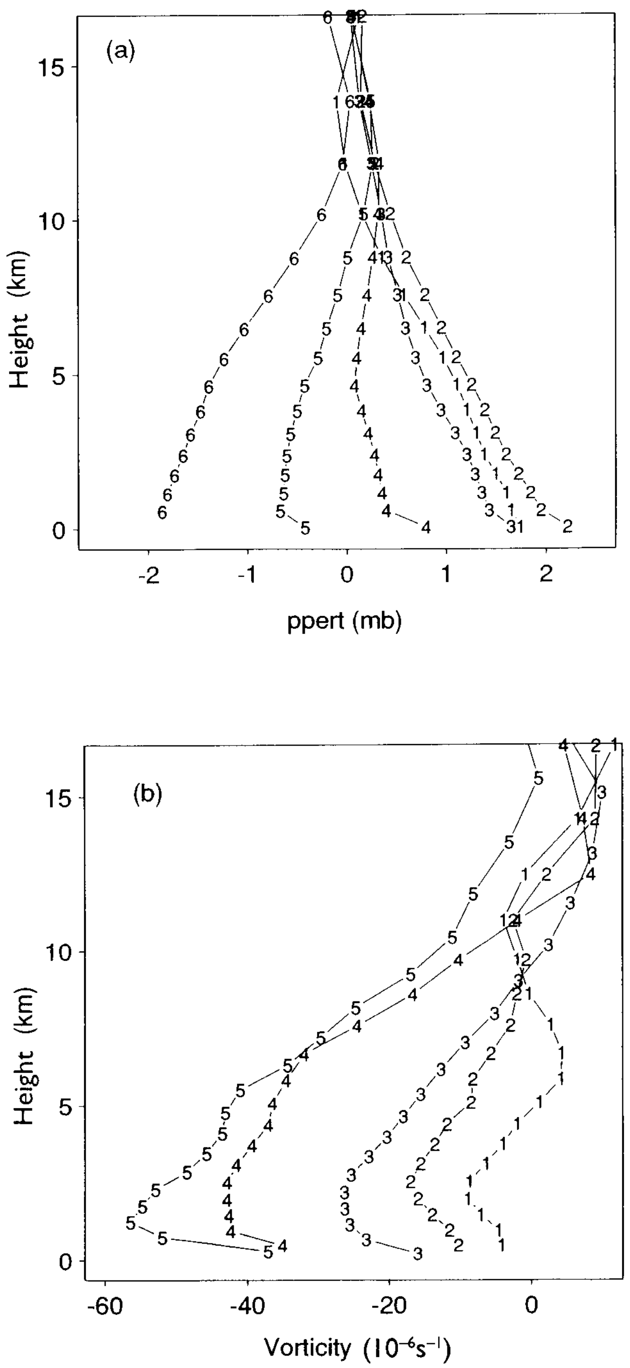

Figure 14. (a) Pressure perturbations, relative to the ship-mean sounding, for the composite categories described in Fig. 13. (b) Composite daily-mean vorticity within the Gulf of Carpentaria sounding array (heavy dashed pentagon in Fig. 1). The categories are defined by daily percentage high cloudiness (infrared temperature $< -55\,^{\circ}\mathrm{C}$) in a square area 600 km on a side centred in the Gulf: category 1: 0–5%; 2: 5–10%; 3: 10–20%; 4: 20–30%; 5: >30%.

of persistent low-level convergence into areas of MCS heating. A similar warm core and low-pressure structure would presumably accompany a (very hypothetical) synoptic-scale cyclone, with vorticity structure like that in Fig. 14(b), but created through the action of the force-curl term of Eq. (2), with no local heating involved at all.

This implies that the impact of MCSs on the larger-scale flow can be profitably viewed as divergence rather than heating *per se*; i.e. as a small-scale 'mass source', a function of height or θ, with a nearly zero mass-weighted vertical integral (some water mass falls out as precipitation). Since the temperature varies little, vertical motion compensates diabatic heating (Charney 1963), so by mass continuity, divergence is related to the vertical gradient of heating (Q in degrees per unit time) in pressure coordinates ($\operatorname{div} \mathbf{V} = -\partial\omega/\partial p \sim -\partial(Q/\sigma)/\partial p$, where σ is the static stability parameter $T(\partial\theta/\partial p)/\theta$). The utility of focusing on divergence, a measurable quantity, as opposed to heating, is a major theme of Part II and of Mapes (1992a).

5. THE EMEX MCSs IN SYNOPTIC CONTEXT

In this section we address the third of the three issues addressed in this paper: the down-scale influence of the synoptic-scale wind field on the mesoscale structure of the MCSs. Data from the EMEX flights are presented below to illustrate the basic processes important to the dynamics of the MCSs. This section summarizes our comprehensive examination of airborne radar reflectivity data, Doppler radar data and dual-Doppler analyses of wind and divergence, *in situ* measurements from multiple aircraft and dropwindsondes, as well as satellite, sounding, and synoptic data*.

All of the EMEX MCSs, except possibly EMEX 2, can be considered to have been in the mature to late stages of the typical mesoscale-system life cycle (Leary and Houze 1979) during the aircraft sampling. Widespread areas of convective and stratiform precipitation had already developed before the flights, and the areal coverage and intensity of new convection decreased during the later parts of the flights. However, within the mature phase of the mesoscale systems, precipitation areas in all phases of a precipitation-feature life cycle (Leary and Houze 1979) were sampled: new convective cells, mature convective cells, transitional forms, and various types and ages of stratiform areas, occasionally including precipitation falling from sheared-over anvil clouds as well as from decaying convection.

The sampling strategy by which these measurements were obtained was identical on each flight. A set of pre-planned flight-pattern templates was employed, according to which the P3 flight track consisted of zigzags composed of straight legs approximately 75 km in length, at 60° angles to each other, at about 5 km altitude. The Electra and F27 flew straight legs back and forth across convective regions, and L-shaped patterns in stratiform areas, at various altitudes below 5 km, with the F27 sampling focused on the boundary layer. The aircraft sampling strategy is discussed in more detail by Webster and Houze (1991), and it will be well illustrated in the examples presented below.

Take-off time on all flights was predawn local time (1700–1900 GMT), to take advantage of the climatological early morning maximum in oceanic high-cloud cover in this part of the world (Williams and Houze 1987; Keenan *et al.* 1989). Landing times were about 8 h later, near local midday (0100–0300 GMT the following day). All times and dates below are GMT; Darwin local time may be obtained by adding 9 h 30 min.

---

* An extended version of this section with much more information on all ten EMEX MCSs may be found in Mapes (1992b). The EMEX 4 rainband has been described by Ryan *et al.* (1992), and case studies of the MCSs of EMEX flights 2, 8 and 9 are in preparation by various researchers.

The precipitation patterns in the MCSs sampled during the ten flights of the EMEX aircraft are indicated schematically in Fig. 15. Streamlines of mid-level synoptic flow in Fig. 15 indicate the relationship of the MCSs to the larger-scale flow features. The adjective 'mid-level' refers to the 550–600 mb level, where the P3 gathered wind observations, but wind direction was generally very similar through the lower half of the troposphere, above the boundary layer. The notation EMEX 1–EMEX 10 indicates the P3 aircraft mission number (flight locations indicated in the inset of Fig. 1). The other aircraft participating in each EMEX flight mission varied; this information can be found in Webster and Houze (1991).

The synoptic wind environments within which MCSs were sampled by the EMEX aircraft can be grouped into four categories:

(i) weak cyclonic depression, weak wind (EMEX 6, 7),
(ii) strong depression/hurricane rainbands (EMEX 4, 5),
(iii) straighter winds outside a strong depression area (EMEX 3, 8, 9, 10), and
(iv) fringes of the monsoon (EMEX 1, 2).

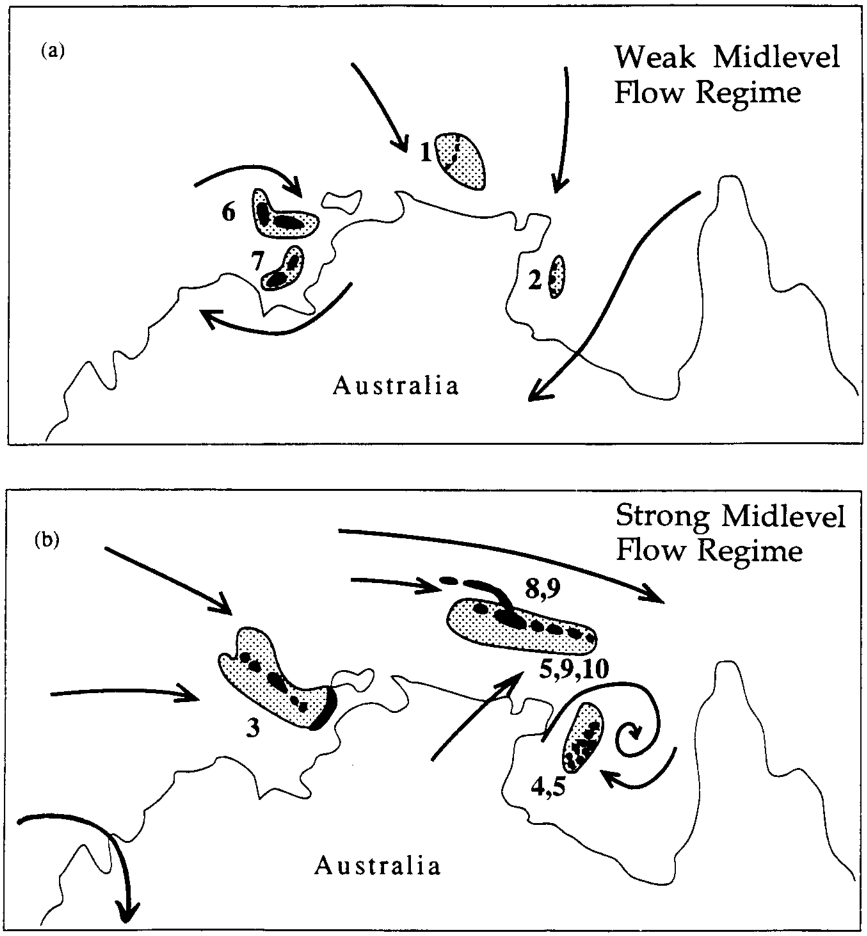

Figure 15. Schematic guide to the EMEX MCSs relative to mid-level flow streamlines. Light outlines represent radar-echo boundaries; convective areas are black, while stratiform precipitation areas are stippled. In panel (a) a weak-wind regime is depicted, while panel (b) represents the strong-wind regime.

Within each wind-regime category the mesoscale organization of the MCSs was broadly similar. In every case, the mesoscale structure consisted of an ensemble of convective lines and stratiform regions, much like the tropical oceanic MCSs of GATE (Houze and Betts 1981) and MONEX (Johnson and Houze 1987). As in those studies, lines of convection in EMEX were found to be generated along the edges of boundary-layer cold pools, and to evolve into stratiform precipitation areas. The particular 4-dimensional patterns assumed by the convective and stratiform parts of the MCSs depended upon the prevailing larger-scale wind fields within which the MCSs occurred. For example, when winds were weak, the stratiform precipitation evolved in place from earlier convection, while in cases with cross-line shear above the melting level, overhanging anvils were formed by the sheared advection of hydrometeors. In some cases these anvils were observed to precipitate. The location and motion of cold-pool boundaries, and hence the triggering of new convection, also depended on environmental wind conditions.

(*a*) *Weak depression MCSs*

The weak cyclonic depression MCSs were characterized by very broad, deep bands of convective clouds. This convection apparently had large upward mass flux, owing to the large horizontal size of the updraughts. Figure 16 shows the best example from EMEX, an updraught which exceeded 1 m s^{-1} continuously along 40 km of flight distance. This flight track was generally along a convective line, but not a particularly narrow one, according to the radar reflectivity pattern. Similar observations of a very broad updraught in an eastern Atlantic depression were presented by Zipser and Gautier (1978). Vertical incidence airborne Doppler-radar data indicate that the level of maximum vertical velocity in this convection was in the upper troposphere, suggesting that such broad updraughts remained undiluted enough to be positively bouyant through most of the troposphere. The updraught temperature exceeded environmental values, according to reliable radiometric measurements, and it was transporting westerly (approximately along-line) momentum upward (Fig. 16). Echo tops within the depression MCSs were very high (16–17 km), and deep long-lived stratiform precipitation areas were observed

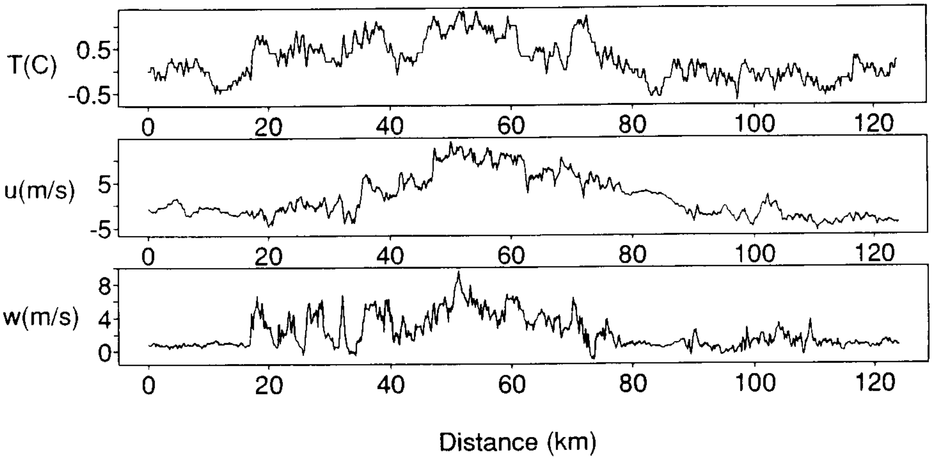

Figure 16. Time-series data from the P3, collected during a flight leg obliquely through a broad convective line during EMEX flight 7, with time converted to distance assuming 135 m s^{-1} ground speed: radiometric temperature, T, (0·7 °C bias correction added; not affected by wetting, so relative values are reliable in rain), zonal wind, u, and vertical wind, w.

to evolve from the initial convection, in the same geographical area, since winds were relatively light.

In the stratiform areas of both of the depression MCSs, cyclonic vorticity concentrated at mid levels was observed. In the EMEX 6 MCS, this vorticity existed in the form of a shear line, while in the case of EMEX 7, a quasi-balanced cyclonic vortex was observed at and above the melting level in the stratiform precipitation area. This vortex is illustrated in Fig. 17, which is an analysis of P3-measured *D*-value (geopotential height perturbation) with *in situ* and Doppler-radar wind measurements superimposed. A hole can be seen in the reflectivity pattern in the vicinity of the vortex (14·3°S, 120°E in Fig. 18(a)), which lies in a stratiform precipitation area south-east of a decaying convective line. The cross-section of Doppler-radar data through the vortex shows that the circulation was localized at and above the melting level (Fig. 18(c)). Mid-level vortices associated with MCS stratiform areas are a frequent observation, both in the tropics (e.g. Houze 1977; Gamache and Houze 1985) and in mid latitudes (e.g. Leary and Rappaport 1987; Brandes 1990). They have been extensively studied with models (e.g. Zhang and Fritsch 1988; Chen and Frank 1992).

(*b*) *Strong depression/hurricane rainbands*

Two EMEX flights (EMEX 4 and 5) sampled precipitation systems in the vicinity of cyclone Irma. During EMEX 4, Irma was not yet of hurricane strength. A rainband

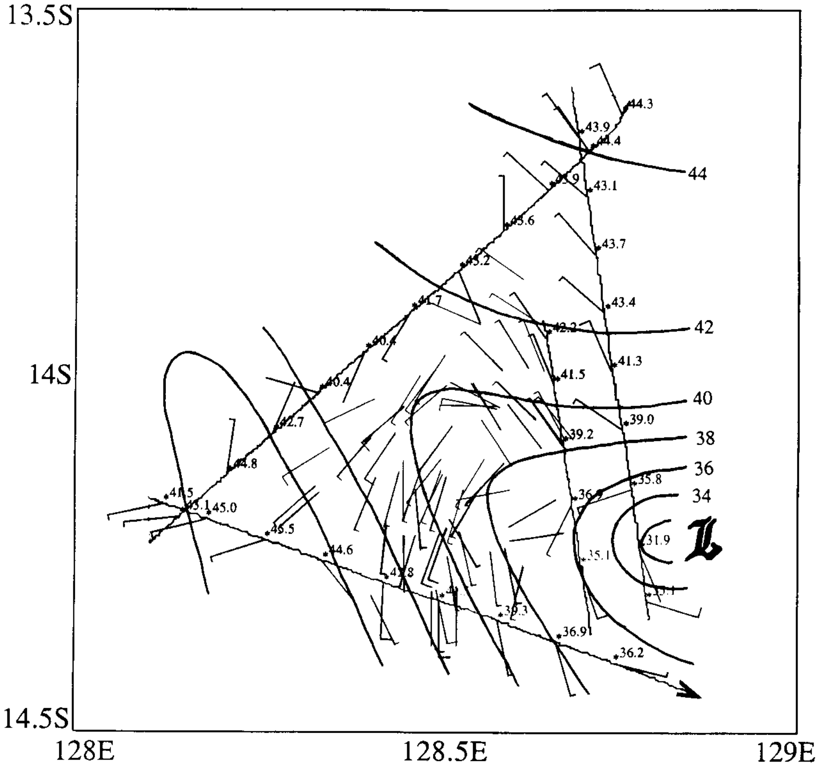

Figure 17. Mid-level mesolow analysis, from P3 data, 2342 GMT 29 January to 0025 GMT 30 January, at 6·5 km altitude. Shown along the solid flight track (with turns excluded) are 1 min mean winds (heavy barbs) and *D*-value (plotted along flight track and contoured at 2 m intervals, absolute value arbitrary). Also shown are Doppler-derived mean winds in 6–7 km layer (light barbs), calculated from pairs of Doppler measurements obtained during three pairs of adjacent flight legs centred at 2342 GMT, 0004 GMT, and 0014 GMT.

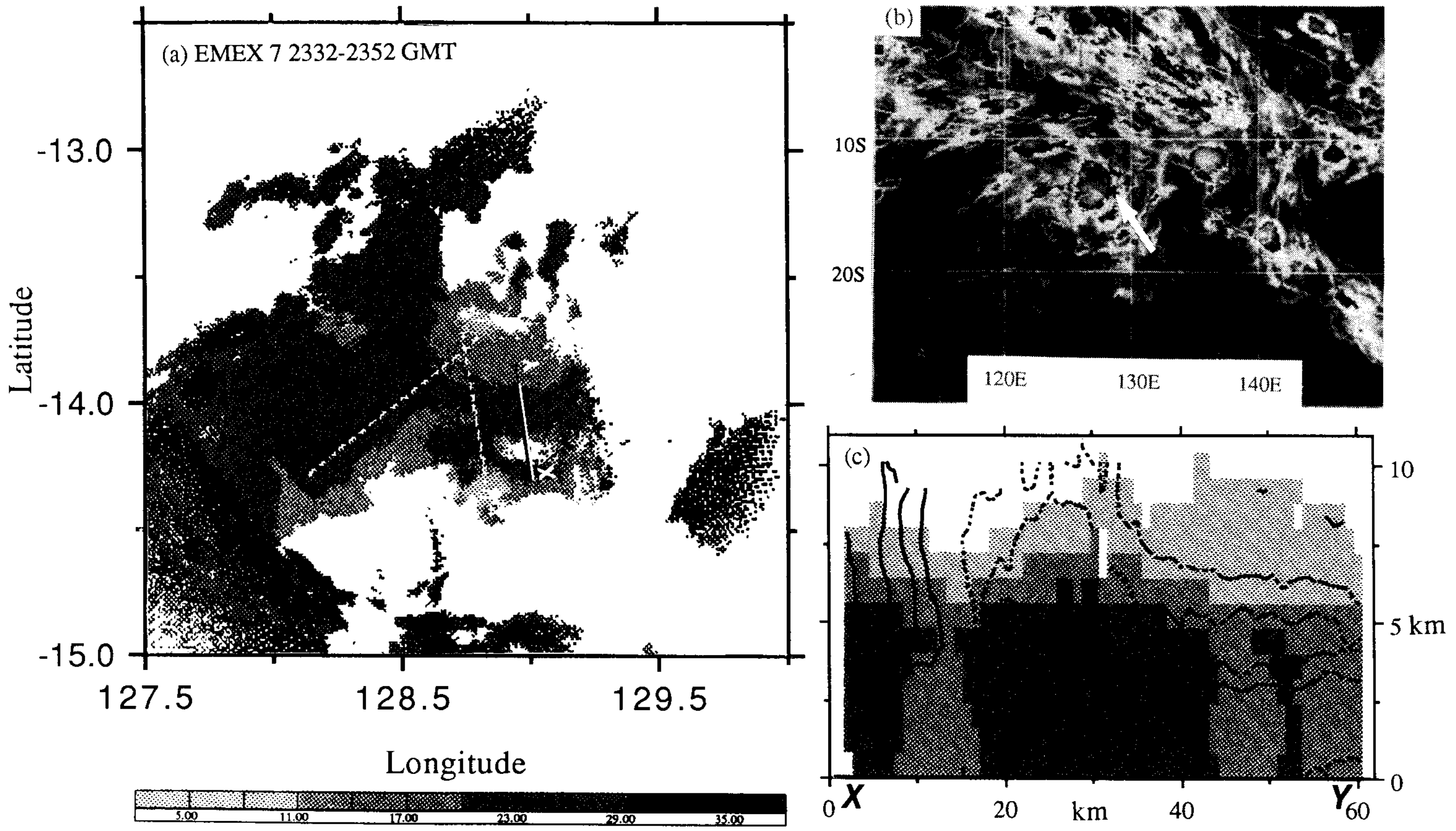

Figure 18. (a) Radar reflectivity from 2332–2352 GMT 29 January, altitude 6·5 km (ground clutter rings the southern edge). (b) Infrared satellite picture at 00 GMT 30 January, enhanced at −55 °C. (c) Vertical cross-section of Doppler-radar data through vortex centre, along line segment XY in radar image (a). Doppler radial-velocity contours (+/− 2, 4, 6 m s^{-1}, where solid lines denote velocities toward the aircraft) overlaid on radar reflectivity image.

at roughly 250 km radius was sampled by the three EMEX aircraft. Like the hurricane rainbands at similar radii studied by Powell (1990a), it consisted of a wide, spirally oriented zone undergoing convection in an environment of strong cross-band shear through the lower troposphere. The resulting vertical transports of momentum made for very turbulent winds at mid levels, and the reflectivity fields were shredded and complex, with generally sharper, cellular reflectivity features on the inner and upwind edges of the band and increasingly stratiform reflectivity fields toward the downwind end of the band. A case study of this rainband is in press (Ryan *et al.* 1992).

The EMEX 5 MCS was something of a hybrid between a cyclone rainband and straight-flow MCS, and for this reason it has been indicated in both places on Fig. 15. It was farther from the centre of Irma than the EMEX 4 band, in the confluence zone between curved streamlines around the cyclone and straighter winds beyond (Fig. 19). The satellite picture in Fig. 19 indicates that this MCS was separate from Irma's core-area convection, and was instead part of a separate synoptic-scale mean cloudiness maximum, north-west of the cyclone centre, that persisted even after cyclone landfall (Fig. 7(c)). The EMEX 5 MCS had somewhat weaker cross-band shear and more lineal convective structures than the hurricane rainband of EMEX 4, but it was none the less

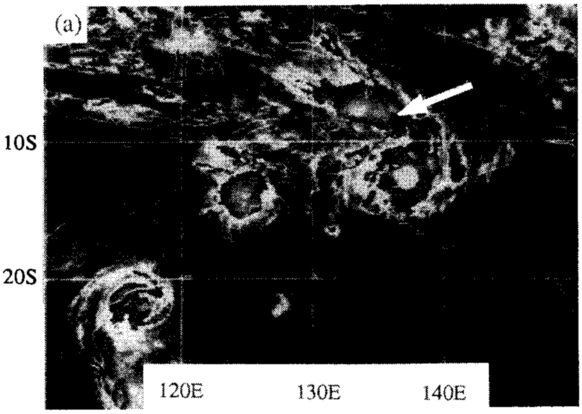

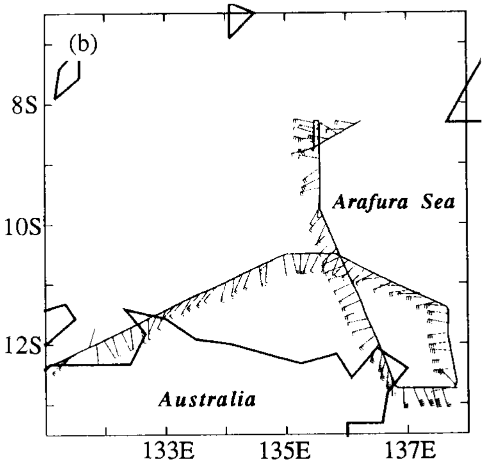

Figure 19. EMEX 5: (a) infrared satellite picture 00 GMT 20 January, enhanced at −55 °C; (b) winds along the P3 flight track (long vane 5 m s^{-1}, short vane 2·5 m s^{-1}), with continental outline (heavy line).

a broad zone of precipitation, spirally oriented with respect to Irma, just at the edge of Irma's pressure field, with multiple embedded convective structures.

(*c*) *Straight, strong winds*

The straight-flow MCSs exhibited two distinct types of linear organization: long, wide along-wind bands, and shorter, narrower cross-wind squalls. The along-wind lines tended to drift slowly northward (outward with respect to the relevant synoptic cyclone), while the squalls moved rapidly eastward (downwind). We will first illustrate the structure and dynamics of the along-wind lines, then show examples of the squalls and the role they sometimes play in the discrete propagation of the along-wind lines. In the interest of brevity, we focus mainly on EMEX 8, 9, and 10, three back-to-back flights into similar nocturnal MCSs over the Arafura Sea during the *long zonal fetch* period.

The largest along-wind line was observed during EMEX 10. At the time of the flight a connected line of high cloudiness ($T_{\mathrm{BB}} < -55\,^\circ\mathrm{C}$) spanned over 1000 km, from 130–140°E at 10°S (Fig. 20(b)). Satellite data viewed in time lapse show that the western portion formed along the north Australian coast the previous evening, while the eastern portion moved north out of the Gulf of Carpentaria. The portion of the line sampled by aircraft consisted of a wide SW-NE band of precipitation with east–west convective line segments within it (Fig. 20(a)). The whole system moved slowly toward the north, with stratiform precipitation both ahead of and behind the convection.

The stratiform precipitation behind (to the south of) the line evolved from old convection, and had higher reflectivity near the surface. In contrast, the stratiform area ahead of the line had higher reflectivity aloft and higher reflectivity top heights (Fig. 21), but lower reflectivity at low levels. It was apparently sheared off from the convection by rear-to-front relative winds above the melting level. Similar leading anvil clouds were observed in EMEX 3 and 8, and precipitation began during the period of the aircraft sampling. This process was also noted by Houze and Rappaport (1984). Within these leading-anvil stratiform areas, small but intense new convective cells sprouted. They were based in the boundary layer, where F27 measurements indicate that evaporation had cooled and moistened the air almost to saturation, but with its θ_e (and therefore CAPE) still characteristic of pre-convective conditions. This is consistent with the results of Barnes and Garstang (1982) concerning the effect of light rain (without convective downdraughts) on the subcloud layer.

The northward propagation of the along-wind convective bands can be understood in terms of the processes maintaining low-level convergence at the northern edge of the cold pool. The ambient boundary-layer flow, as seen in every one of 22 dropwindsondes from EMEX 3, 8, 9, and 10, had a component to the right of the deep westerly current. This is in the Ekman sense (wind veering with height), the boundary-layer flow spiralling inward with respect to the nearest synoptic cyclone. This 'velocity boundary layer' was substantially deeper than the thermodynamic mixed layer (subcloud layer), typically 1–1·5 km or more. This flow could be expected to converge at the northern edge of the cold pool, to the extent that cold-pool air conserved momentum from its mid-tropospheric source region or gained southerly momentum from a pressure-gradient acceleration, while descending in downdraughts.

Evidence of the transport of mid-level southerly momentum into the cold pool by downdraughts can be seen in EMEX 10 data. The P3 data indicate that southerly winds were blowing out of the Gulf, behind the line, at mid levels (Fig. 20), while F27 measurements in the boundary layer indicate that cold air, arriving from mid levels via convective-scale downdraughts, was highly correlated with southerly momentum (Fig. 22). That dynamical interactions may increase the southerly momentum that down-

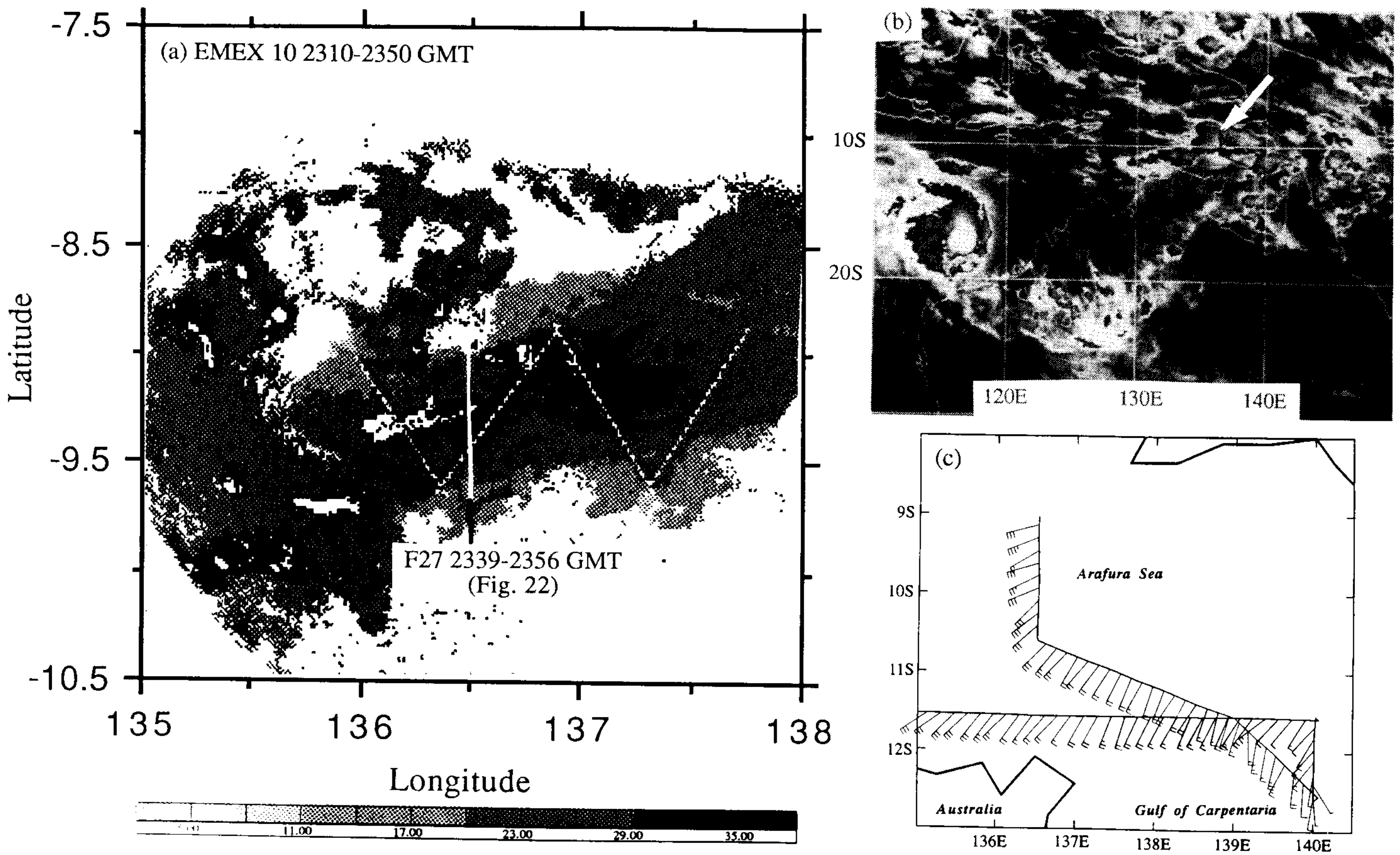

Figure 20. EMEX 10: (a) radar reflectivity time composite from 2310–2359 GMT 3 February, altitude 4·5–5·8 km; (b) infrared satellite picture at 00 GMT 4 February, enhanced at −55 °C; and (c) winds along P3 flight track (long vane 5 m s^{-1}, short vane 2·5 m s^{-1}) and continental outline (heavy line).

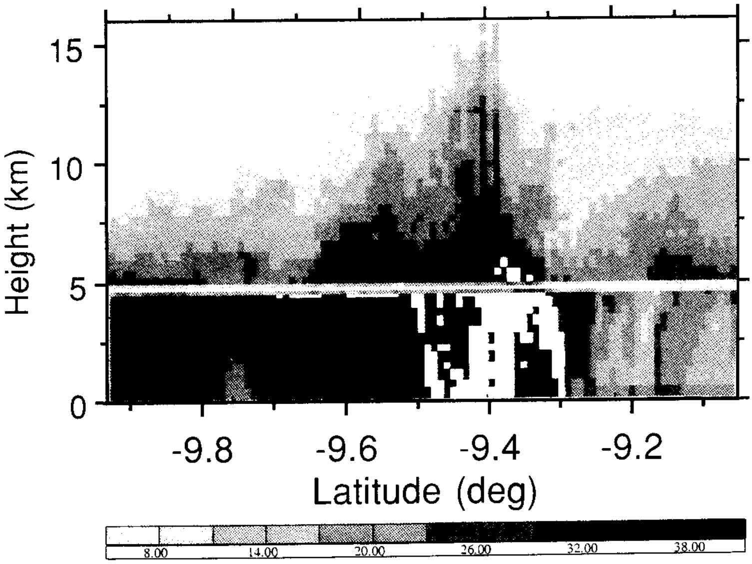

Figure 21. Radar reflectivity cross-section of the EMEX 10 MCS, along 136·5°E, from data taken at 2150–2201 GMT 3 February.

draughts bring into the boundary layer is shown by the Electra-data time series of Fig. 23, which is from a north–south pass through the EMEX 9 MCS described below. The downdraught, south of the updraught, was experiencing a northward (rear-to-front) pressure-gradient force, while the updraught experienced a front-to-rear pressure-gradient force. However, this transection was not necessarily representative of the routine dynamics of along-wind lines, because of its proximity to a squall feature.

In addition to the *continuous* propagation described above, the along-wind lines also moved in discrete steps, modulated by cross-wind squalls. An excellent example of this process was documented in the EMEX 9 MCS, in which a squall arc protruding northward from a pre-existing east–west precipitation band passed rapidly eastward along the band (Fig. 15). The old precipitation band evolved into the 'trailing stratiform precipitation' behind the new E–W 'leading convective line' along the new cold-pool edge laid down by the squall arc (Figs. 12–15 of Webster and Houze 1991). A case study of the EMEX 9 MCS is underway.

A similar process of discrete propagation occurred in EMEX 8. In this case the existing convective line lay initially WNW–ESE along 9·9–10·3°S (Fig. 24(a)). A north-

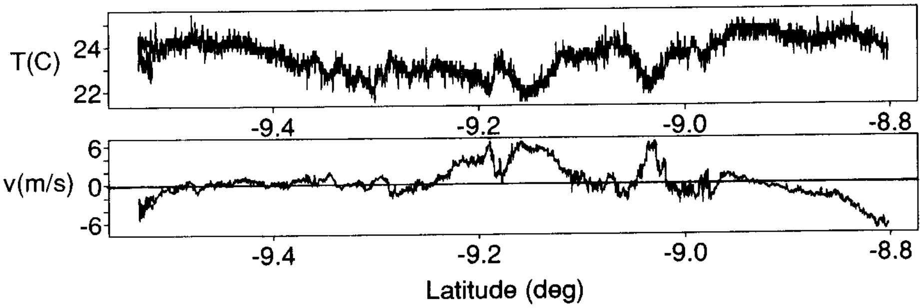

Figure 22. F27 measurements of temperature, T, and meridional wind, v, at 970 mb (350 m altitude) 2339–2356 GMT 3 February during the flight leg indicated on Fig. 20.

ward-jutting stub of convection along 136°E passed rapidly down the band from west to east, with the most intense convection always near the intersection point between these two features. In the wake of this squall, a northward migration of the cold-pool boundary was observed by the F27, accompanied by some other transient convective activity. By 00 GMT (Fig. 24(b)), a new, tidy line of convection had reformed along the advanced position of the cold-pool edge, along 9·5°S, while the old convective line had evolved into stratiform precipitation. The snapshot in Fig. 24(b) appears to exhibit the leading-line/trailing-stratiform structure seen in many squall lines (e.g. Houze 1977; Zipser 1977). However, the stratiform precipitation in this case was a product of the *in situ* evolution of earlier convection, not of the sheared advection of hydrometeors from a quasi-steady convective line, as in the mid-latitude squall line studied by Biggerstaff and Houze (1991).

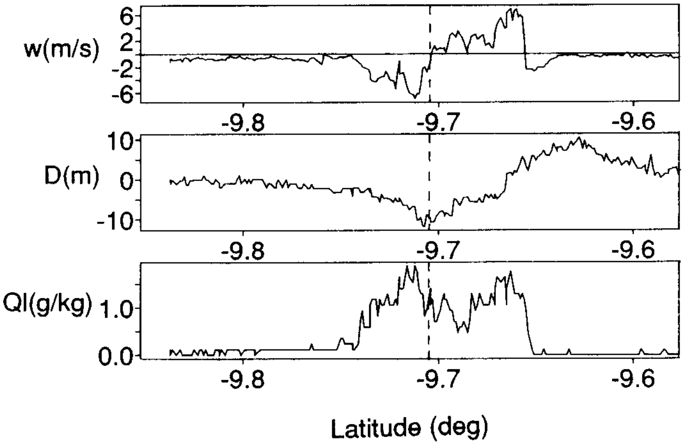

Figure 23. Electra measurements of vertical velocity, w, D-value perturbation (proportional to geopotential height), and liquid water mixing ratio, Q_l, from the PMS forward scattering probe, at 695 mb 2131–2135 GMT 2 February, during a northbound flight leg along 138·1°E, crossing a convective line from rear (downdraught) to front (updraught).

(*d*) *Fringes of the monsoon*

The EMEX 1 and 2 MCSs require separate treatment, not because they are inconsistent with the above categorizations, but because they were marginal to the monsoon and not in their mature stages during aircraft sampling. The EMEX 1 MCS lay out at the fringe of the monsoonal cloudy area, in relatively weak flow. The precipitation area was decaying, and was already shallow, weak, and mostly stratiform when the aircraft arrived. The only convection observed was an embedded arc of weak, short cells (<10 km top height) at the leading edge of a mesoscale pulse of westerly wind, centred above the boundary layer, at 2 km altitude (Fig. 25). Weak but sharp-edged updraughts, measured by the Electra, confirmed that buoyant convection was taking place. However, its base was above the boundary layer, and the inertia of the elevated jet, rather than a boundary-layer cold-pool boundary, appears to have been the agent of lifting which triggered the convection.

The EMEX 2 MCS, by contrast, was a young, stationary line of sporadic convective cells with little stratiform precipitation. It lay in the Gulf of Carpentaria, in easterly flow, entirely outside the satellite-observed monsoonal cloudy area. Intensive multiple-aircraft sampling was performed within a small spatial area, but this small MCS did not appear to be a very significant part of the monsoon system. Very late in the flight, a more solid

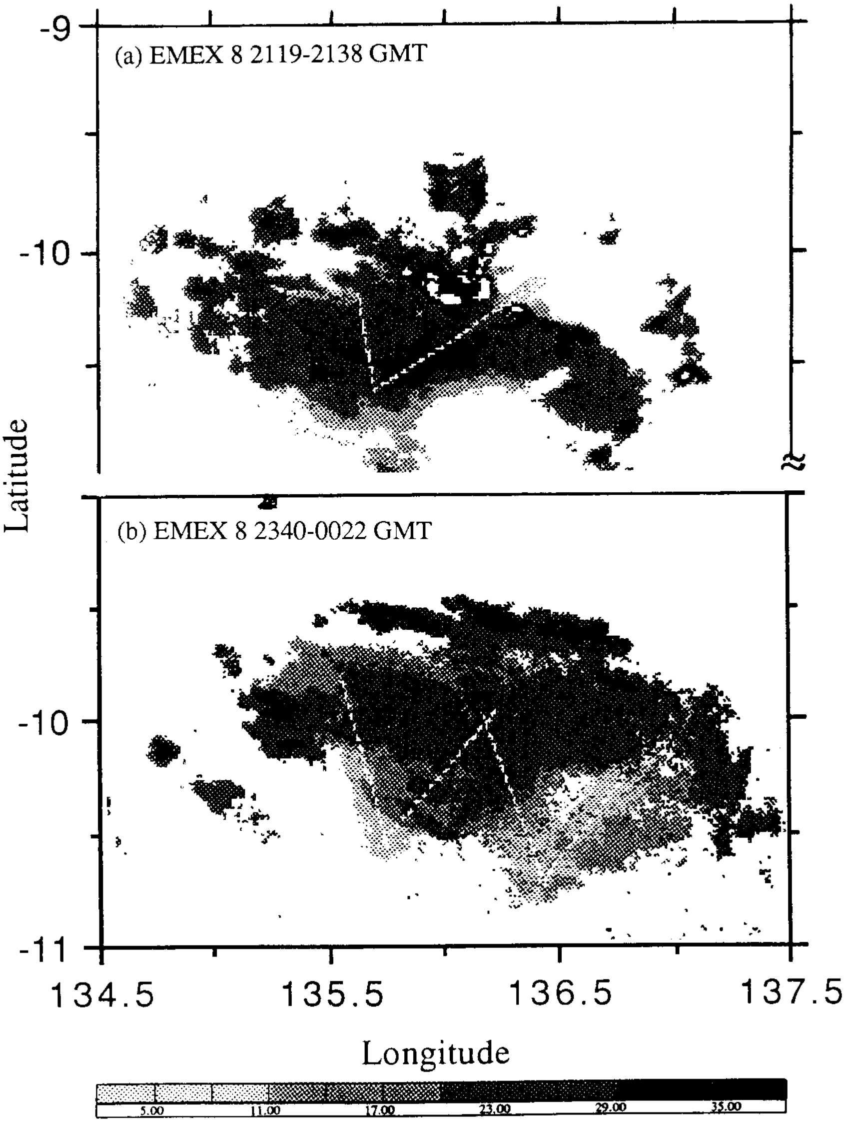

Figure 24. EMEX 8 radar reflectivity time composites. Upper panel: 2119–2138 GMT 1 February, altitude 4·8 km. Lower panel: 2340 GMT 1 February–0022 GMT 2 February, altitude 5·8–6·2 km.

convective line structure developed, with stratiform precipitation behind the convective line and a significant pressure perturbation field.

6. CONCLUSIONS

The 1987 Australian monsoon's precipitating convection occurred primarily near the Australian coast, but offshore (Fig. 5) over the world's warmest waters (Fig. 9). The monsoon appears to be an unstable, positive-feedback process in which deep convection, once triggered, favours additional deep convection. Tropical cyclones, spun up by the aggregate effect of the deep convection, persist until landfall or poleward drift extinguish

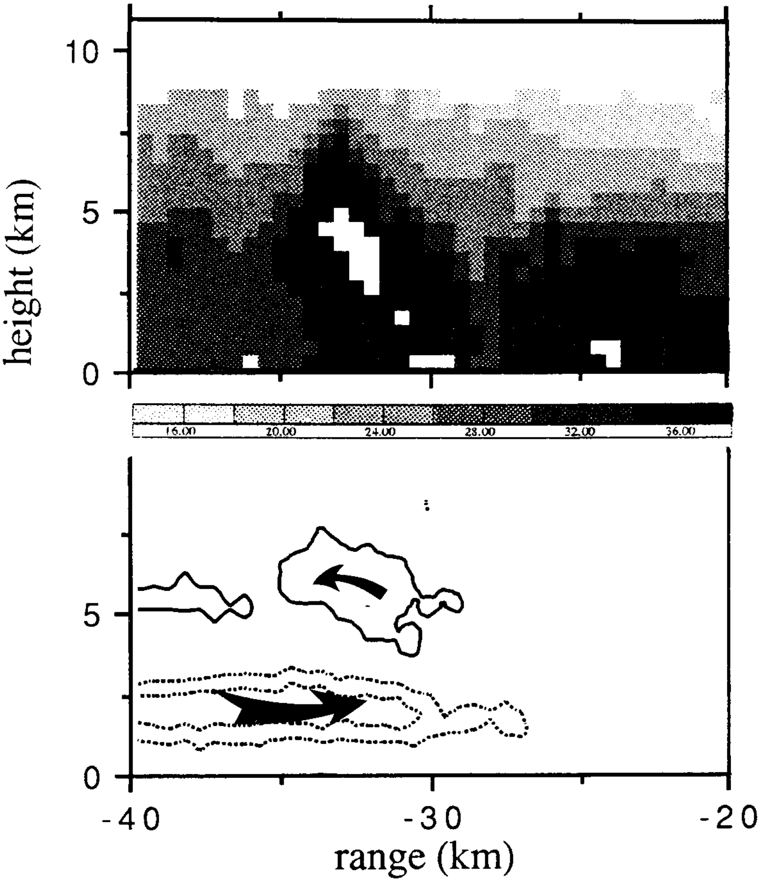

Figure 25. Doppler-radar cross-section of weak convective line in EMEX 1. Top: radar reflectivity; bottom: Doppler radial velocity (contours at +/−3 and 6 m s^{-1}).

them. Two such cycles of activity, with two cyclones in each cycle, were observed during the 1987 AMEX–EMEX field program.

The forcing of larger-scale monsoon flow by embedded deep convection is expressed by two source terms in an equation for large-scale absolute vorticity. The first term, of primary importance, reflects 'vortex stretching' by the mean low-level convergence associated with *net* MCS heating. Because the divergent flow extends out to large distances, localized convective heating spins up not only mesoscale vortices and tropical cyclones but also the large-scale monsoon circulation. The second term, the curl of a force vector reflecting vertical momentum transports in convection, creates vorticity couplets in the upper troposphere, flanking the area in which the momentum transports are localized. These vorticity couplets have no net circulation at larger scales.

Low-level cyclonic vorticity over Australia is accompanied by lower surface pressures (heuristically indicated in Fig. 14), while upper-tropospheric pressure variations are much smaller. Therefore, the upper troposphere becomes warmer as the monsoon trough strengthens (Fig. 13). The decrease in sampled pressure variation with height arises from the different spatial scales of the upper-tropospheric divergent outflow and its near-zero absolute-vorticity anticyclone on the one hand, and the smaller cyclonic lows in the convergent lower levels on the other, as might be expected from gradient-wind considerations.

Even though the upper-tropospheric temperature increase reduces the buoyancy and CAPE of ascending boundary-layer air parcels, the warmer, cyclonic environments are observed to contain more convective activity. This observation suggests that monsoon deep convection, like that in easterly waves, is modulated by low-level processes, not by the destabilizing effects of some hypothetical deep forced ascent.

Such low-level processes mostly act as positive feedbacks. Evaporation enhancement by convectively induced surface winds (on many spatial scales), and humidification of the dry troposphere by convection, may favour later convection. Boundary-layer cold pools in MCSs trigger additional convection through intense low-level lifting at their edges, yet are readied by surface fluxes to undergo deep ascent in only half a day or so. Monsoonal MCS heating induces a lifted boundary layer in a mesoscale area around the heating (Mapes 1992a). Low surface pressure causes convergence of the frictional boundary-layer flow. In short, convection favours more convection nearby in myriad ways, given a suitable supply of heat and moisture. As a result, the active phases of the monsoon, once initiated, can be viewed as 'superclusters' of overlapping, interacting deep convection, which at any given instant are composed of distinct individual MCSs.

The MCSs of the Australian monsoon are apparently much like those observed elsewhere, in that they consist of convective areas, generally aligned along boundary-layer cold-pool edges, and areas of stratiform precipitation, which mostly evolved from earlier convection. The basic processes of MCS dynamics—the regeneration of convection along cold-pool edges, and the evolution of stratiform precipitation from prior convection—seem to be common to all MCSs. In the EMEX aircraft program, MCSs were observed in three distinct monsoon low-level wind regimes: quiescent or weak depression environments, tropical cyclones, and strong straight-wind environments. Within each wind regime, the MCSs had similar characteristics, as summarized in Fig. 15.

The MCSs in weak-depression environments were characterized by broad, deep convective structures (e.g. Fig. 16), which evolved in place into long-lasting stratiform precipitation areas, in which mid-level cyclonic vorticity maxima were observed (Figs. 17 and 18). In stronger depression and tropical-cyclone environments, hurricane rainband-type MCSs were observed: broad spiral bands of precipitation with multiple embedded convective structures. In strong, straight flow, two distinct forms of organization were observed: large along-wind lines, and smaller cross-wind-oriented squalls. The along-wind lines moved slowly outward (relative to the synoptic trough or cyclone) as new convection grew along the outer side, fed at low levels by the veering frictional boundary-layer flow. The smaller squall features moved rapidly downwind, and in some cases acted to cause a discrete propagation or 'jump' of the along-wind lines (Fig. 24). In all the MCSs, stratiform precipitation was observed to evolve from previous convection.

In summary, the Australian monsoon system consists of a series of self-amplifying episodes of widespread deep convection, in the form of mesoscale convective systems, whose structures depend systematically on the larger-scale monsoon flow, itself a result of spin-up by the aggregate divergent circulations of all the foregoing MCSs.

ACKNOWLEDGEMENTS

Sounding data for this study were provided by the Australian Bureau of Meteorology. Ray Zehr of CIRA, Colorado State University, supplied the satellite data. G. C. Gudmunson edited the original manuscript. This work was supported by the US NOAA Hurricane Research Division and National Science Foundation, under NSF grant ATM9008406.

REFERENCES

Aspliden, C. I. 1976 A classification of the structure of the tropical atmosphere and related energy fluxes. *J. Appl. Meteorol.* **15,** 692–697

Barnes, G. M. and Garstang, M. 1982 Subcloud layer energetics of precipitating convection. *Mon. Weather Rev.*, **110,** 102–117

Betts, A. K. 1974 Thermodynamic classification of tropical convective soundings. *Mon. Weather Rev.*, **102,** 760–764

Biggerstaff, M. I. and Houze Jr., R. A. 1991 Kinematic and precipitation structure of the 10–11 June 1987 squall line. *Mon. Weather Rev.*, **119,** 3034–3065

Brandes, E. A. 1990 Evolution and structure of the 6–7 May 1985 mesoscale convective system and associated vortex. *Mon. Weather Rev.*, **118,** 109–127

Charney, J. G. 1963 A note on large-scale motions in the tropics. *J. Atmos. Sci.*, **30,** 1100–1111

Charney, J. G. and Eliassen, A. 1964 On the growth of the hurricane depression. *J. Atmos. Sci.*, **21,** 68–75

Chen, S. S. and Frank, W. M. 1992 A numerical study of the genesis of extratropical convective mesovortices. Part I: Evolution and dynamics. *J. Atmos. Sci.*, In Press

Cho, H.-R. and Jenkins, M. A. 1987 The thermal structure of tropical easterly waves. *J. Atmos. Sci.*, **44,** 2531–2539

Cho, H.-R., Cheng, L. and Bloxam, R. M. 1979 The representation of cumulus cloud effects in the large-scale vorticity equation. *J. Atmos. Sci.*, **36,** 127–139

Davidson, N. E., Holland, G. J., McBride, J. L. and Keenan, T. D. 1990 On the formation of AMEX cyclones Irma and Jason. *Mon. Weather Rev.*, **118,** 1981–2000

Dudhia, J. and Moncrieff, M. W. 1987 A numerical simulation of quasi-stationary tropical convective bands. *Q. J. R. Meteorol. Soc.*, **113,** 929–967

Emanuel, K. A. 1986 An air–sea interaction theory for tropical cyclones. Part I: Steady state maintenance. *J. Atmos. Sci.*, **43,** 585–604

1987 An air–sea interaction model of intraseasonal oscillations in the tropics. *J. Atmos. Sci.*, **44,** 2324–2340

Esbensen, S. K., Shapiro, L. J. and Tollerud, E. I. 1987 The consistent parameterization of the effects of cumulus clouds on the large-scale momentum and vorticity fields. *Mon. Weather Rev.*, **115,** 664–669

Fitzjarrald, D. R. and Garstang, M. 1981 Boundary-layer growth over the tropical ocean. *Mon. Weather Rev.*, **109,** 1762–1772

Gamache, J. F. and Houze Jr., R. A. 1985 Further analysis of the composite wind and thermodynamic structure of the 12 September GATE squall line. *Mon. Weather Rev.*, **113,** 1241–1259

Gamache, J. F., Marks Jr., F. D. and Burpee, R. W. 1987 EMEX data report: The Equatorial Mesoscale Experiment. AOML/HRD Report, National Oceanic and Atmospheric Administration, Atlantic Oceanographic and Meteorological Laboratory, Hurricane Research Division, 4301 Rickenbacker Causeway, Miami, FL 33149, USA

Gaynor, J. E. and Ropelewski, C. F. 1979 Analysis of the convectively modified GATE boundary layer using *in situ* and acoustic sounder data. *Mon. Weather Rev.*, **107,** 985–993

Gill, A. E. 1980 Some simple solutions for heat-induced tropical circulation. *Q. J. R. Meteorol. Soc.*, **106,** 447–462

Gunn, B. W., McBride, J. L., Holland, G. J., Keenan, T. D. and Davidson, N. E. 1989 The Australian summer monsoon circulation during AMEX Phase II. *Mon. Weather Rev.*, **117,** 2554–2574

Haynes, P. H. and McIntyre, M. E. 1987 On the evolution of vorticity and potential vorticity in the presence of diabatic heating and frictional or other forces. *J. Atmos. Sci.*, **44,** 828–841

1990 On the conservation and impermeability theorems for potential vorticity. *J. Atmos. Sci.*, **47,** 2021–2033

Hendon, H. H. and Liebmann, B. 1990 A composite study of the onset of the Australian summer monsoon, *J. Atmos. Sci.*, **47,** 2227–2240

Hendon, H. H., Davidson, N. E. and Gunn, B. W. 1989 Australian summer monsoon onset during AMEX 1987. *Mon. Weather Rev.*, **117,** 370–390

Holland, G. J. 1986 Interannual variability of the Australian summer monsoon at Darwin: 1952–82. *Mon. Weather Rev.*, **114,** 594–604

Houze Jr., R. A. 1977 Structure and dynamics of a tropical squall-line system. *Mon. Weather Rev.*, **105,** 1540–1567

Houze Jr., R. A. and Betts, A. K. 1981 Convection in GATE. *Rev. Geophys. Space Phys.*, **19,** 541–576

Houze Jr., R. A. and Rappaport, E. N. 1984 Air motions and precipitation structure of an early summer squall line over the eastern tropical Atlantic. *J. Atmos. Sci.*, **41,** 553–574

Houze, Jr., R. A., Geotis, S. G., Marks, Jr., Churchill, D. D. and Herzegh, P. H. 1981 Comparison of airborne and land-based radar measurements of precipitation during winter MONEX. *J. Appl. Meteorol.*, **20,** 772–783.

Janowiak, J. E. and Arkin, P. A. 1991 Rainfall variations in the tropics during 1986–1989, as estimated from observations of cloud-top temperature. *J. Geophys. Res.*, **96,** 3359–3374

Johnson, R. H. and Houze Jr., R. A. 1987 Precipitating cloud systems of the Asian monsoon. Pp. 298–353 in *Monsoon meteorology*. Eds. C. P. Chang and T. N. Krishnamurti. Oxford University Press

Johnson, R. H. and Kriete, D. C. 1982 Thermodynamic and circulation characteristics of winter monsoon tropical mesoscale convection. *Mon. Weather Rev.*, **110,** 1898–1911

Jorgensen, D. P. 1984 Mesoscale and convective-scale characteristics of mature hurricanes. Part I: General observations by research aircraft. *J. Atmos. Sci.*, **41,** 1268–1285

Keenan, T. D. and Brody, L. R. 1988 Synoptic-scale modulation of convection during the Australian summer monsoon, *Mon. Weather Rev.*, **116,** 71–85

Keenan, T. D., McBride, J., Holland, G., Davidson, N. and Gunn, B. 1989 Diurnal variations during the Australian Monsoon Experiment (AMEX) Phase II. *Mon. Weather Rev.*, **117,** 2535–2552

Leary, C. A. and Houze Jr., R. A. 1979 The structure and evolution of convection in a tropical cloud cluster. *J. Atmos. Sci.*, **36,** 437–457

Leary, C. A. and Rappaport, E. N. 1987 The life cycle and internal structure of a mesoscale convective complex. *Mon. Weather Rev.*, **115,** 1503–1527

Lindzen, R. S. and Hou, A. Y. 1988 Hadley circulations for zonally averaged heating centered off the equator. *J. Atmos. Sci.*, **45,** 2416–2427

Mapes, B. E. 1992a Gregarious tropical convection. *J. Atmos. Sci.*, in revision

1992b 'The Australian monsoon and its mesoscale convective systems'. Ph.D. dissertation, University of Washington

McBride, J. L. 1987 The Australian monsoon. Pp. 203–230 in *Monsoon meteorology*. Eds. C. P. Chang and T. N. Krishnamurti. Oxford University Press

Neelin, J. D., Held, I. M. and Cook, K. H. 1987 Evaporation–wind feedback and low-frequency variability in the tropical atmosphere. *J. Atmos. Sci.*, **44,** 2341–2348

Nicholls, M. E. and Johnson, R. H. 1984 A model of a tropical squall line boundary layer wake. *J. Atmos. Sci.*, **41,** 2774–2792

Nicholls, M. E., Pielke, R. A. and Cotton, W. R. 1991 Thermally forced gravity waves in an atmosphere at rest. *J. Atmos. Sci.*, **48,** 1869–1884

Ogura, Y. and Yoshizaki, M. 1988 Numerical study of orographic-convective precipitation over the eastern Arabian sea and the Ghat mountains during the summer monsoon. *J. Atmos. Sci.*, **45,** 2097–2122

Powell, M. D. 1990a Boundary layer structure and dynamics in outer hurricane rainbands. Part I: Mesoscale rainfall and kinematic structure. *Mon. Weather Rev.*, **118,** 891–917

1990b Boundary layer structure and dynamics in outer hurricane rainbands. Part II: Downdraft modification and mixed layer recovery. *Mon. Weather Rev.*, **118,** 918–938

Ramage, C. S. 1971 *Monsoon meteorology*. Academic Press, New York

Reed, R. J. and Recker, E. E. 1971 Structure and propagation of synoptic-scale wave disturbances in the equatorial western Pacific. *J. Atmos. Sci.*, **28,** 1117–1133

Riehl, H. and Malkus, J. S. 1958 On the heat balance in the equatorial trough zone. *Geophysica*, **6,** 503–538

Rutledge, S. A., Williams, E. R. and Keenan, T. D. 1992 The Down Under Doppler and Electricity Experiment (DUNDEE): Overview and preliminary results. *Bull. Am. Meteorol. Soc.*, in Press

Ryan, B. F., Barnes, G. M. and Zipser, E. J. 1992 A wide rainband in a developing tropical cyclone. *Mon. Weather Rev.*, in Press

Sardeshmukh, P. D. and Hoskins, B. J. 1987 On the derivation of the divergent flow from the rotational flow: the χ problem. *Q. J. R. Meteorol. Soc.*, **113,** 339–360

Sui, C.-H. and Yanai, M. 1986 Cumulus ensemble effects on the large-scale vorticity and momentum fields of GATE. Part I: Observational evidence. *J. Atmos. Sci.*, **41,** 1618–1642

Thompson Jr., R. M., Payne, S. W., Recker, E. E. and Reed, R. J. 1979 Structure and properties of synoptic-scale wave disturbances in the intertropical convergence zone of the eastern Atlantic. *J. Atmos. Sci.*, **36,** 53–72

Tollerud, E. I. and Esbensen, S. K. 1983 An observational study of the upper-tropospheric vorticity fields in GATE cloud clusters. *Mon. Weather Rev.*, **111,** 2161–2175

Webster, P. J. 1987 The elementary monsoon. Pp. 3–32 in *Monsoons*. Eds. J. S. Fein and P. L. Stephens. Wiley Interscience

Webster, P. J. and Houze Jr., R. A. 1991 The Equatorial Mesoscale Experiment (EMEX): An overview. *Bull. Am. Meteorol. Soc.*, **72,** 1481–1505

Williams, M. and Houze Jr., R. A. 1987 Satellite-observed characteristics of winter monsoon cloud clusters. *Mon. Weather Rev.*, **115,** 505–519

Xu, K.-M. and Emanuel, K. A. 1989 Is the tropical atmosphere conditionally unstable? *Mon. Weather Rev.*, **117,** 1471–1479

Zhang, D.-L. and Fritsch, J. M. 1988 A numerical investigation of a convectively generated inertially stable warm-core mesovortex over land. Part I: Structure and evolution. *Mon. Weather Rev.*, **116,** 2660–2687

Zipser, E. J. 1977 Mesoscale and convective-scale downdrafts as distinct components of squall-line circulation. *Mon. Weather Rev.*, **105,** 1568–1589

Zipser, E. J. and Gautier, C. 1978 Mesoscale events within a GATE tropical depression. *Mon. Weather Rev.*, **106,** 789–805